

PHYS3003 Report: First Semester, 2020
“New high-redshift radio galaxy candidates from GLEAM”

Nigel Wright (ID: 18003330)

Supervisors: Nick Seymour; Jess Broderick

June 5, 2020

Abstract

Radio galaxies are some of the largest and most luminous objects in the Universe. High-redshift ($z > 2$) radio galaxies provide valuable information about the early Universe, including galaxy evolution and the local environment of an expanding Universe.

The most distant radio galaxy currently known has a redshift of $z = 5.72$ (Saxena et al., 2018a). This project is part of a wider research effort currently underway to efficiently select ultra-high-redshift radio galaxies via a new selection method that utilises parameters not fully covered by previous surveys. The presence of such massive galaxies in the first billion years of the Universe ($z > 6$) would challenge notions of galaxy evolution and provide unique opportunities to study the Epoch of Reionisation.

This report presents the background, methodology and preliminary results of that research effort, which involved visual inspection of 165 radio galaxy candidates at near-infrared wavelengths. It also empirically derives several important characteristics of radio galaxies, which are presented here, concluding with an outline of further work scheduled for Semester 2, 2020.

Contents

1	Introduction	6
1.1	Aim	6
1.2	This Report	7
2	Background	8
2.1	Radio Galaxies	8
2.2	Radio-loud AGN	9
2.3	High-redshift radio galaxies	12
2.4	$K-z$ relation	14
2.5	Luminosity at high redshifts	16
2.6	Previous Surveys	17
2.6.1	Demographic summary of HzRGs	17
2.7	Common methods of detection and investigation	19
2.7.1	Case studies: TN J0924-2201 and TGSS J1530+1049	20
3	Methodology	22
3.1	Pilot study	22
3.2	Improvements applied to current study	23
3.3	Data sources and Analysis methods	24
3.3.1	Data sources	24
3.3.2	Analysis methods	25
3.3.3	Analysing HzRG characteristics	25
4	Results	27
4.1	Identifying Near-Infrared Sources	27
4.2	HzRG characteristics	29
4.2.1	$K - z$ Relation	29
4.2.2	Luminosity vs Redshift	30
4.2.3	Radio K -band Flux Ratios	31
5	Discussion	33
5.1	Near-infrared sources	33
5.2	Characteristics of high-redshift radio galaxies	33
5.2.1	$K - z$ Relation	33
5.2.2	Luminosity vs Redshift	34
5.2.3	Radio K -band Flux Ratios	34
6	Conclusions and Future Work	36
6.1	Work completed in Semester 1, 2020	36
6.2	Plans for Semester 2, 2020	36
6.3	Conclusion	36

<i>CONTENTS</i>	2
Acknowledgements	38
Bibliography	39
A VIKING Inspection Data	43

List of Figures

2.1	Cygnus A. An FR II radio galaxy, with radio emission dominated by the large lobes and fuelled by jets emitted from the central core. Imaged at 5 GHz by the Very Large Array (Carilli and Barthel 1996: http://www.aoc.nrao.edu/~ccarilli/cyga.shtml)	8
2.2	M87. An FR I radio galaxy, with peak emission in the jets and core. Imaged by the Very Large Array (Image from https://hubblesite.org/contents/news-releases/1999/news-1999-43.html).	9
2.3	Unification model of active galactic nuclei, according to Urry and Padovani (1995). Note that for radio galaxies, the accretion disk is hidden by the torus, so that it would appear as a normal galaxy at optical and near-infrared wavelengths.	10
2.4	Typical frequency spectra of radio galaxies (3C 84, $z=0.0176$; 3C 123, $z=0.218$) and quasars (3C 48, $z=0.369$; 3C 454.3, $z=0.859$) (Kellermann and Owen, 1988).	12
2.5	Radio spectrum of a typical double radio galaxy, including contributions from various AGN components. Note the secondary x-axes that indicates how the frequencies each component is detected at changes with redshift (Ker et al., 2012).	13
2.6	Panchromatic view of spectral energy distribution of high-redshift radio galaxy 4C 23.56, $z = 2.5$. The spectra has been decomposed into its various components: <i>Cyan</i> : radio synchrotron; <i>Black</i> : Absorbed non-thermal X-Ray AGN; <i>Yellow</i> : nebular continuum; <i>Blue</i> : AGN-heated thermal dust emission; <i>Red</i> : Starburst-heated dust emission; <i>Green</i> : stars; <i>Magenta</i> : scattered quasar (Miley and De Breuck, 2008).	14
2.7	K -band sequences for elliptical and spiral galaxies, plotted against models of galaxy mass functions generated by the PEGASE.2 galaxy mass simulation (Rocca-Volmerange et al., 2004).	15
2.8	Spiderweb galaxy (MRC 1138-262). With a redshift of $z = 2.2$, this large radio galaxy is in the process of merging with numerous satellite galaxies (Miley and De Breuck, 2008). The blue contours are Ly α , with showing a gaseous nebula surrounding the cluster, and the red contours from 8GHz radio data and indicate non-thermal radio emission.	18
4.1	GLEAM J090906–010227 (Sources from L-R: VLASS, FIRST, VIKING. Note: Synthesized beam in bottom left-hand corner). Note the lack of infrared counterpart to radio source, shown by overlaying the pink VLASS contours onto the VIKING image (right panel). Selected for further investigation.	27
4.2	GLEAM J092123+013834 (Sources from L-R: VLASS, FIRST, VIKING. Note: Synthesized beam in bottom left-hand corner). Double radio source. Note the presence of a K -band counterpart in the left most contours. Not selected for further investigation.	28

4.3 GLEAM J114641–000734 (Sources from L-R: VLASS, FIRST, VIKING. Note: Synthesized beam in bottom left-hand corner). Extended/Double radio source. Not selected for further investigation.	28
4.4 GLEAM J143727+014303 (Sources from L-R: VLASS, FIRST, VIKING. Note: Synthesized beam in bottom left-hand corner). Slightly extended radio source with no K -band counterpart. Selected for further investigation.	28
4.5 K - z relation of a sample of HzRGs (log scale). Markers are sized according to their luminosity, with large markers indicating $L_{500} > 10^{27}$ W Hz $^{-1}$. Also plotted are PEGASE.2 K -magnitude tracks for initial galaxy mass functions, at three different formation redshifts.	29
4.6 K - z relation of a sample of HzRGs, with $z > 1$. Markers are sized according to their luminosity, with large markers indicating $L_{500} > 10^{27}$ W Hz $^{-1}$. Also plotted are PEGASE.2 K -magnitude tracks for initial galaxy mass functions, at three different formation redshifts.	30
4.7 Luminosity (L_{150}) vs Redshift (log scale). Markers are sized according to their spectral index, with large markers indicating $\alpha < -1.2$	30
4.8 Luminosity (L_{150}) vs Redshift, $z > 1$. Markers are sized according to their spectral index, with large markers indicating $\alpha < -1.2$	31
4.9 K flux ratios at S_{150} , including QSOs. Markers are sized according to their luminosity, with large markers indicating $L_{150} > 10^{27}$ W Hz $^{-1}$	31

List of Tables

3.1	Selection criteria. (Note: ¹ ELAIS S1 too far south for DR2; ² This study)	23
3.2	Radio and Infrared Survey data used to identify infrared counterparts of radio sources. VLASS and VIKING datasets were used for each comparison, with the secondary radio source varying in accordance with survey coverage.	24
4.1	Results of visual inspection of radio-infrared imaging.	27
A.1	G1_EQU_GAMA (VLASS, FIRST, VIKING).	44
A.2	G1_EQU_not_GAMA (FIRST, VIKING).	45
A.3	G2_SGP_GAMA_VIKING (ASKAP, GLASS, VIKING).	47

Chapter 1

Introduction

High-redshift radio galaxies are some of the most massive, highly luminous objects in the Universe. The study of high-redshift radio galaxies (HzRGs) began with Minkowski's (1960) redshift measurement of 3C 295, which at $z = 0.462$ was the most distant object known.

The field expanded with large-scale radio surveys in the 1960s, 1970s and 1980s, through programs like the Cambridge Radio Surveys (see the review papers by McCarthy 1993 and Miley and De Breuck 2008 for further details). Today, the most distant radio galaxy has a redshift of $z = 5.72$ (Saxena et al., 2018a), when the Universe was only 1 Gyr old.

1.1 Aim

The original intent of this project was to assist researchers at CIRA who had developed a novel selection technique for efficiently finding HzRGs, using spectral curvature at low radio frequencies $\lesssim 250$ MHz and a standard cut in near-infrared K -band ($2.2\ \mu\text{m}$) magnitude. A pilot study of this technique resulted in the discovery of the second-most distant radio galaxy at $z = 5.55$ (Drouart et al., 2020). It was hoped a large-scale investigation would identify radio galaxies at redshifts $z > 6$, placing them firmly in the Epoch of Reionisation when the Universe was less than one billion years old. This project was designed to assist the team with their investigation, while building experience in academic research, data analysis, tools and techniques in radio astronomy.

Making use of the Years 1 and 2 Galactic and Extragalactic All-sky Murchison Widefield Array survey catalogues (Wayth et al. 2015; Hurley-Walker et al. 2017; Franzen et al. in prep.) observed with the Murchison Widefield Array (Tingay et al. 2013), HzRG candidates were examined in near-infrared K -band imaging from the ESO VISTA Kilo-degree Infrared Galaxy (VIKING) survey (Edge et al. 2013), and other high resolution radio survey data catalogues.

This project was interrupted in March 2020 by the global COVID-19 pandemic. As social distancing policies were implemented across the world, telescope observations were limited or postponed and the project was forced to pivot to a more academic focus. As a result, HzRG candidate selection and multi-wavelength followup was forced to halt until further resources became available.

1.2 This Report

This report was written as an assessment piece for PHYS3003 (Physics Project 1). It is intended as an end-of-semester progress report for a year-long project titled “New high-redshift radio galaxy candidates from GLEAM”, supervised by Dr Nick Seymour and Dr Jess Broderick at the Curtin Institute of Radio Astronomy (CIRA).

The layout of this paper is as follows. In Chapter 2, we define high-redshift radio galaxies, their physical and observational characteristics. We conclude this chapter with a summary of previous surveys and common methods of detecting and investigating them. In Chapter 3, we present the methodology behind a new method of detecting high-redshift radio galaxies, based on a pilot study by Drouart et al. (2020). More specifically to this project, a subset of that investigation is presented here as a small part of the larger research effort. Chapter 4 presents preliminary results, highlighting high-redshift radio galaxy candidates found thus far, and Chapter 5 analyses what these potential high-redshift candidates may represent. Chapter 6 concludes with next steps for the project and plans for second semester 2020.

Throughout this report, we assume a flat Λ CDM cosmology with Hubble constant, $H_0 = 67.7$ km/s/Mpc and matter density parameter, $\Omega_M = 0.307$. These parameters are taken from the first Planck cosmological data release (Planck Collaboration 2016).

Chapter 2

Background

2.1 Radio Galaxies

In the decades after the Second World War, several large-scale radio surveys were carried out to map the radio sky. These surveys identified thousands of radio sources, many of which were later identified as originating from outside our own galaxy, the Milky Way.

In 1951, Cygnus A (3C 405) was identified as the first radio galaxy with a redshift of 0.056 (Baade and Minkowski 1954). Cygnus A (Figure 2.1) displays features that typify radio galaxies, with two large radio lobes ejected from a small yet bright galactic core, powered by an active galactic nucleus (AGN), which is now known to be a super massive black hole (SMBH). The radio lobes extend far into intergalactic space, often spanning hundreds of kiloparsecs.

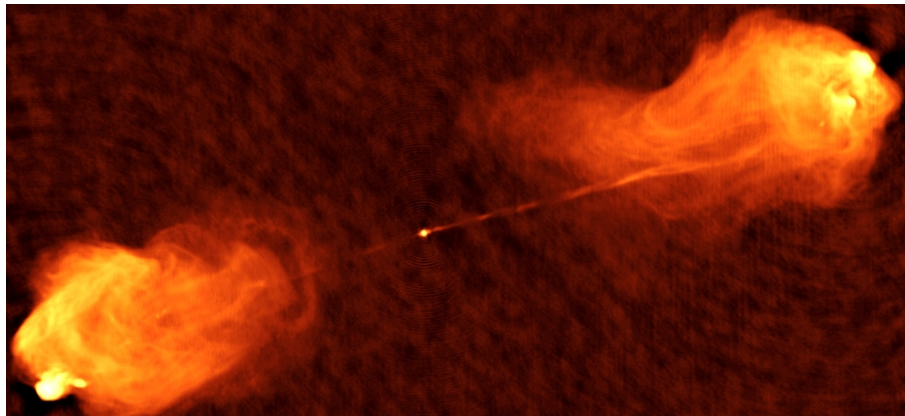


Figure 2.1: Cygnus A. An FR II radio galaxy, with radio emission dominated by the large lobes and fuelled by jets emitted from the central core. Imaged at 5 GHz by the Very Large Array (Carilli and Barthel 1996: <http://www.aoc.nrao.edu/ccarilli/cyga.shtml>).

Minkowski's 1960 redshift measurement of 3C 295 was later followed by the first radio galaxy with a redshift greater than 1 (Spinrad 1982: 3C 368, $z = 1.13$). A few years later, Chambers et al. (1988) found radio galaxies with redshifts over 2 (4C 40.36, $z = 2.269$) and other surveys soon found redshifts of 3 and greater. Currently, the most distant radio galaxy is TGSS J1530+1049 at a redshift of $z = 5.72$ (Saxena et al. 2018a), with a small number of galaxies at similar distances, including GLEAM 0856 at $z = 5.55$ (Drouart et al. 2020) and TN J0924-2201 at $z = 5.19$ (van Breugel et al. 1999).

As shown in Figure 2.1, the lobes of a radio galaxy dwarf the central core by many scales of magnitude. Based on the appearance and brightness of the lobes of a radio galaxy, Fanaroff and Riley (1974) devised a two-category classification system: Fanaroff-Riley II (FR II) radio sources

describe the most powerful radio galaxies, like Cygnus A, which display “edge-brightened” outer lobes and hot spots. Relatively less luminous sources are classified as Fanaroff-Riley I (FR I) radio galaxies (Figure 2.2), where the peak emission is in the jets and cores.

As well as differences based on appearance, the FR types can also be separated by luminosity. FR II sources have 1.4 GHz luminosity $L_{1.4\text{GHz}} > 10^{25} \text{ W Hz}^{-1}$, in comparison with FR I sources, which have $L_{1.4\text{GHz}} > 10^{23-25} \text{ W Hz}^{-1}$ (Burke, Graham-Smith and Wilkinson, 2019). High-redshift radio galaxies are typically FR II type radio sources.

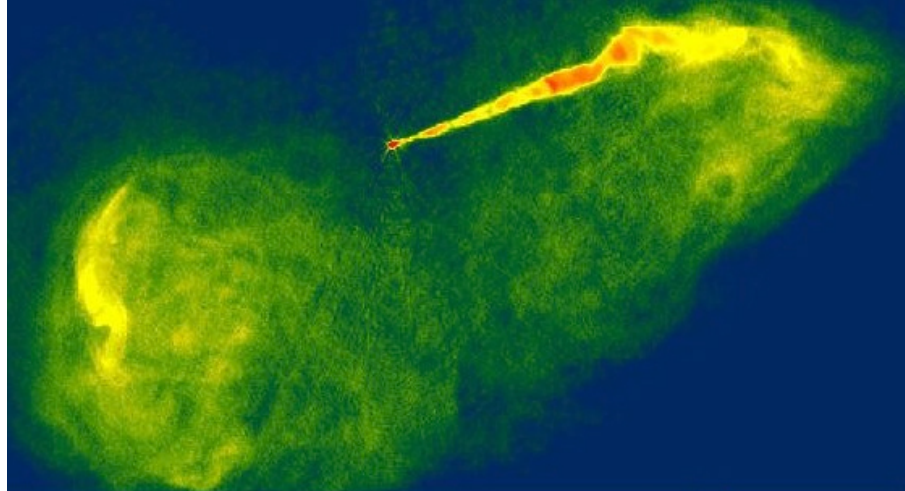


Figure 2.2: M87. An FR I radio galaxy, with peak emission in the jets and core. Imaged by the Very Large Array
(Image from <https://hubblesite.org/contents/news-releases/1999/news-1999-43.html>).

Similar to the Fanaroff-Riley classification system, radio galaxies above $L_{1.4\text{GHz}} > 10^{23} \text{ W Hz}^{-1}$ are classified as radio loud (Burke, Graham-Smith and Wilkinson, 2019), with sources below this luminosity classified as radio quiet. At lower redshifts, radio loud galaxies have been positively identified with giant elliptical gE and cD galaxies, suggesting that high-redshift radio galaxies represent these massive galaxies in their early stages of formation. In their study on HzRG morphology, van Breugel et al. (1998) found some indication that the host galaxies of FR II sources are ellipticals that exhibit evidence of relatively recent galaxy interactions.

Despite (or perhaps because of) their large luminosities, radio galaxies are rare. Roughly 10% of all known galaxies can be classified as AGN, and of these, a further 10% are bright enough to be classified as radio-loud (Saxena et al., 2018b).

2.2 Radio-loud AGN

Radio galaxies are powered by active galactic nuclei (AGN), which are stronger emitters than the nuclei of “normal” galaxies (like our own Milky Way). The strongly emitting part is unrelated to star formation and is generally accepted to be connected to the presence of an accreting SMBH ($M_{\text{BH}} > 10^6 M_{\odot}$). Two massive jets of relativistic plasma are launched from the AGN into intergalactic space, where they dissipate and form lobes hundreds of kiloparsecs across. Such jets are fundamentally linked with strong radio sources and are dominated by synchrotron radiation (Burke, Graham-Smith and Wilkinson, 2019).

Within the broad classification of AGN lie many different types of galaxies, including Seyfert galaxies, quasars, blazars and radio galaxies. Padovani et al. (2017) identified 51 different classes of AGN in their review of the existing literature, although they attribute most of these differences to four main parameters: orientation to the observer, accretion rate, the presence or absence of strong jets, and the host galaxy and its environment (Figure 2.3).

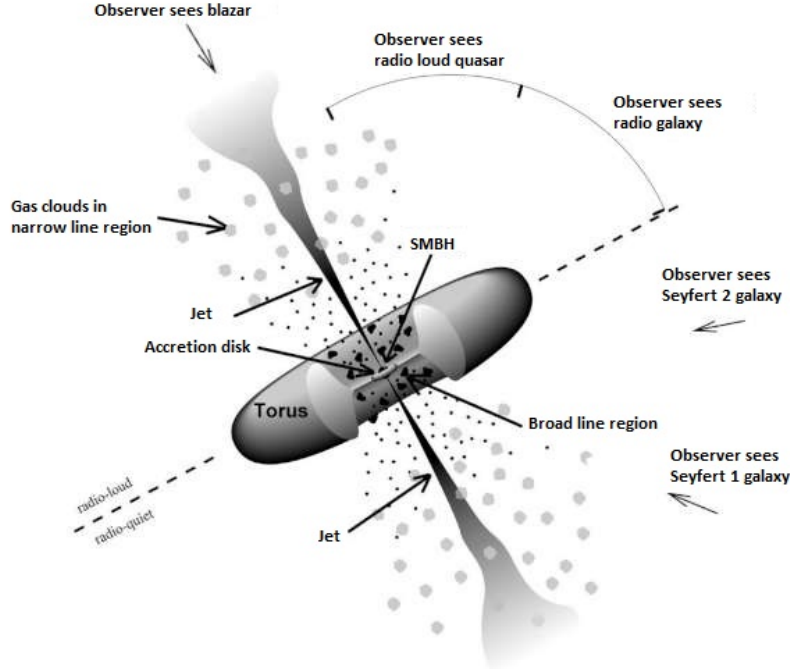


Figure 2.3: Unification model of active galactic nuclei, according to Urry and Padovani (1995). Note that for radio galaxies, the accretion disk is hidden by the torus, so that it would appear as a normal galaxy at optical and near-infrared wavelengths.

As illustrated in Figure 2.3, when a radio galaxy is observed, the associated quasar is believed to be either hidden from view or highly variable and observed when the quasar is in a dormant state (Miley and De Breuck, 2008).

AGN consist of several components, with the size of each component varying by many scales of magnitude to each other (Padovani et al., 2017). These include:

- Black holes ($10^{-7} - 10^{-3}$ pc)
- Accretion disk ($10^{-7} - 1$ pc)
- Dusty torus (1 – 10 pc)
- Jet ($10^{-7} - 10^6$ pc)
- Host Galaxy and Dark Matter halo ($10 - 10^6$ pc).

Radio loud AGN ($L_{1.4\text{GHz}} > 10^{23} \text{ W Hz}^{-1}$) emit a significant fraction of energy non-thermally and are associated with relativistic jets, while radio quiet AGN are dominated by thermal emission, related to the SMBH accretion disk (Padovani et al. 2017). This means both FR I and FR II radio galaxies (FR I: $L_{1.4\text{GHz}} > 10^{23-5} \text{ W Hz}^{-1}$, FR II: $L_{1.4\text{GHz}} > 10^{25} \text{ W Hz}^{-1}$) are radio loud.

There are three main classes of radio-loud AGN: Blazars, Quasars and Radio Galaxies (Burke, Graham-Smith and Wilkinson, 2019). Blazars are flat spectrum sources, with jets oriented at very small angles (less than 15-20 degrees) with respect to line of sight (Padovani et al. 2017). Quasars are also classified as being FR I or FR II sources, although with quasars the bright outer lobes are much less bright than the central component and relativistic jets (Kellermann and Owen 1988). In general, only about 10% of radiation from a quasar is emitted at radio wavelengths, with most being emitted at submillimetre wavelengths (Kellermann and Owen 1988). Radio galaxies occur when the accretion disk of a radio-loud AGN is obscured by the torus, so that it largely appears as a normal galaxy in optical or near-IR.

The typical lifetime of a radio-loud AGN is ~ 100 Myr and the key processes that dominate its lifetime are:

- synchrotron emission in the early stages of radio AGN evolution, which gives rise to the power-law behaviour of low frequency spectral energy distributions
- adiabatic losses when the jet reaches galactic scales (and beyond)
- inverse Compton losses due to interaction with the cosmic microwave background photons at much larger scales.

The ultimate source of energy in an AGN is accretion flow onto the black hole, which is in turn powered by the gravitational potential of the infalling material. Changes in accretion flow are also the most important variable in observational characteristics of an AGN (Padovani et al. 2017). This process of fuelling the central SMBH through accretion, in combination with the effect the energy it produces has on the host galaxy and its intergalactic neighbourhood is known as AGN feedback. AGN feedback plays an important role in the evolution of HzRGs, their morphology and environment (Sanders et al. 1988, but see Padovani et al. 2017). Growth of the SMBH directly influences and regulates the growth of the host galaxy.

The underlying difference between FR I and FR II radio sources is their accretion rates onto the central SMBH. In FR II sources, accretion rates are high, while FR I rates are low (Burke, Graham-Smith and Wilkinson 2019). FR II sources require a significant supply of gas from within their host galaxies to fuel them (or from a merged galaxy).

According to Blandford and Znajek (1977), jet production and collimation is likely to be associated with magnetic fields associated with the SMBH accretion disk. Lobes develop when the jets are stopped by the ram pressure of the diffuse intergalactic gas, causing heat spots of radiation to build up at the diffusion points.

Jets contain particles (mainly electrons) typically of energy about 1 GeV, confined within a weak toroidal magnetic field of 10^{-4} Gauss (Kellermann and Owen 1988). The brightness of a jet is affected by radiation losses, adiabatic gains or losses, and other energy gains or losses associated with relativistic electrons (Kellermann and Owen 1988). Jets in FR II galaxies are generally straight, while less powerful FR I jets are more susceptible to disturbance by changes in the intergalactic medium. If the jet is oriented towards the observer, relativistic beaming causes the jet closest to the observer to appear much brighter than the rearward pointing jet.

The jets of both FR I and FR II-type radio galaxies show strong signs of polarisation, often in excess of 50% or more. In FR I sources, the magnetic fields are perpendicular to the jet axis or perpendicular fields, which change to parallel fields at some point along the jet. FR II sources have magnetic fields parallel to the jet axis all the way along the jet. The lobes of FR II sources have magnetic fields running along the outer edge of the lobes (Kellermann and Owen 1988).

After the early stages of synchrotron losses, the magnetic field strength declines and adiabatic losses begin to dominate (Saxena et al. 2018b). Once the size of the lobe has exceeded the extent of the X-ray halo of the host galaxy, and the energy density of the magnetic field of the lobe is comparable to the energy density of the CMB, losses due to inverse Compton scattering against CMB photons begins to dominate.

Typical radio frequencies used to study AGN range from 10 MHz to a few tens of GHz (Padovani et al. 2017). The dominant emission process in the low frequency radio spectrum is synchrotron emission, where relativistic particles gain or lose energy. Synchrotron emission is usually explained by a power law:

$$S_\nu \approx \nu^\alpha \quad (2.1)$$

where S_ν is the flux density, usually expressed in Jansky (Jy) or milliJansky (mJy) (1 Jansky = $10^{-26} \text{ W m}^{-2} \text{ Hz}^{-1}$) at frequency ν (MHz), with a spectral index α (Kellermann and Owen 1988).

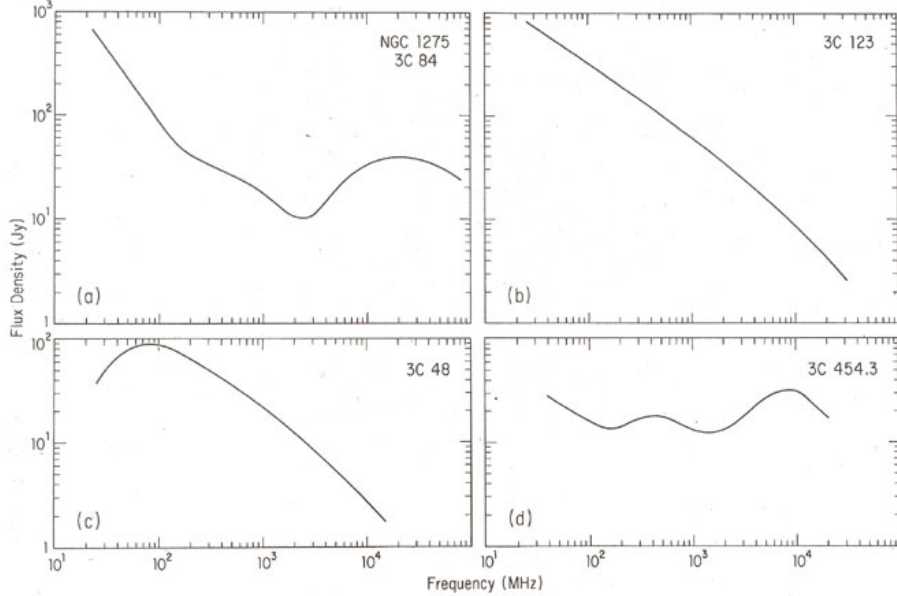


Figure 2.4: Typical frequency spectra of radio galaxies (3C 84, $z=0.0176$; 3C 123, $z=0.218$) and quasars (3C 48, $z=0.369$; 3C 454.3, $z=0.859$) (Kellermann and Owen, 1988).

Radio galaxies can be separated into two main categories, those with steep ($\alpha \leq -0.5$) or flat ($\alpha > -0.5$) spectra. These spectra derive from an intrinsic distribution of electron energies. It should be noted that the actual threshold between “steep” and “flat” varies, but generally, “steep” indicates α less than -0.8 to -0.5, while flat is $\alpha > -0.5$. These categories roughly correspond to extended and compact sources respectively (Padovani et al. 2017). As shown in Figure 2.4, in radio galaxies where lobes dominate (3C 123) and in the low frequency portion of a Seyfert galaxy (3C 84), the radio spectra is steep, with spectral indices less than -0.8. Compact sources such as quasars (3C 48, 3C 454.3) are affected by self-absorption and so their spectra are generally flat (Kellermann and Owen, 1988; Burke, Graham-Smith and Wilkinson, 2019).

2.3 High-redshift radio galaxies

Radio galaxies look very different at low and high-redshifts. In the local Universe, radio galaxies are always hosted by giant elliptical galaxies with a small spread of absolute magnitude (Eales et al. 1997). At high-redshifts, radio galaxies appear in optical wavelengths as a series of knots strung out along the radio axis (Best et al. 1998).

Most radio galaxies detected in low-frequency radio surveys are extended, with projected linear sizes in tens of kiloparsecs to megaparsecs and steep non-thermal spectrum ($\alpha \leq -0.7$). Conversely, most high-frequency radio sources are compact, with typical sizes of $< 1\text{pc}$ and relatively flat spectral indices ($\alpha > -0.4$) (Miley and De Breuck, 2008).

Although they appear very faint at high-redshifts, HzRGs have brighter near-infrared magnitudes and bluer optical-infrared colours than would be expected from their low-redshift equivalents, with high emission-line luminosities and smaller radio sizes (Eales et al. 1997). Emission lines can be used to glean information on the ionisation rate, metallicity and star formation rates of the host galaxy. HzRGs typically display narrow emission lines (FWHM $< 2000 \text{ km/s}$), with a small number exhibiting broad emission lines, which are more commonly found in radio-

loud quasars, where the broad line region of the AGN is directly in the line of sight of the observer.

An important tool in analysing HzRGs are their spectral energy distribution (SED), where frequency is plotted against flux density. Figure 2.5 illustrates the various components of a typical radio galaxy spectrum. If a radio galaxy is not viewed along its jet axis, the emission is dominated at low frequency by synchrotron emission in the radio lobes, which typically display a steep-spectrum power curve.

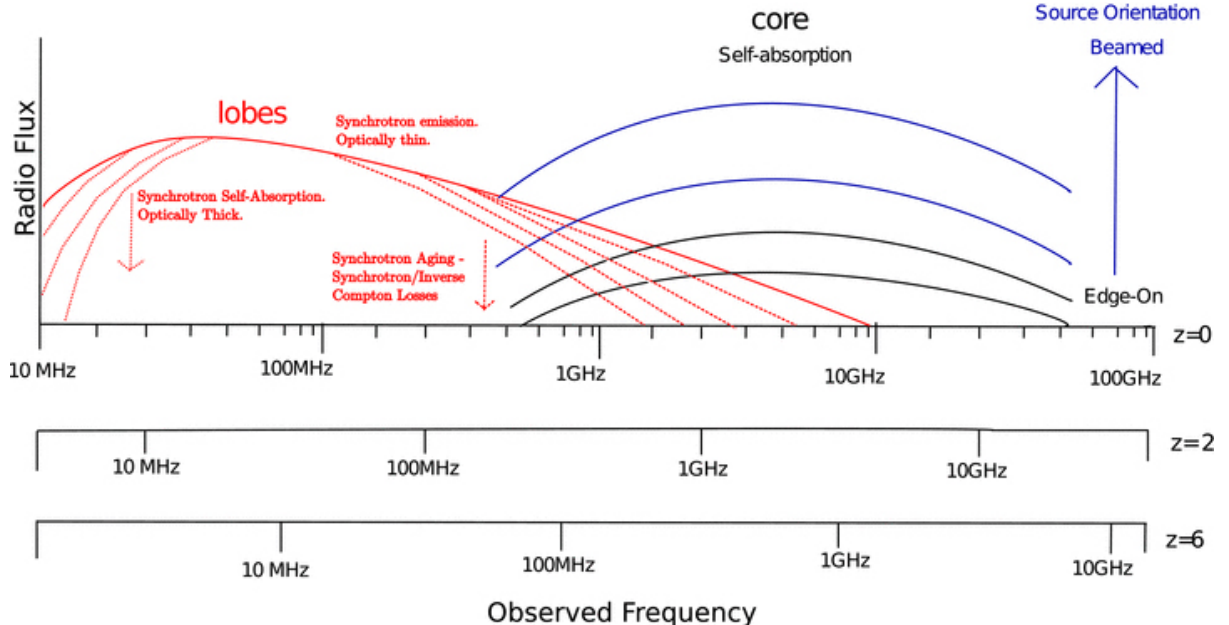


Figure 2.5: Radio spectrum of a typical double radio galaxy, including contributions from various AGN components. Note the secondary x-axes that indicates how the frequencies each component is detected at changes with redshift (Ker et al., 2012).

Power curves can steepen at higher frequencies due to synchrotron and inverse-Compton energy losses. At frequencies $\nu \geq 1\text{GHz}$, the spectrum becomes dominated by the AGN core and is typically flat, as a result of superposition of self-absorbed components of different sizes at the base of the jet. As can be seen in Figure 2.5, the frequency these features will be observed at changes with redshift. This is why low-frequency radio sampling is preferable for investigating high-redshift radio galaxies (Ker et al., 2012), and why lobes are not detected by high-frequency radio surveys.

Figure 2.6 shows the SED of a typical HzRG from radio to X-ray wavelengths, decomposed into its various constituents - relativistic plasma, gas and dust, stars and the AGN. At high energies, spectral flattening or turnover at low radio frequencies is expected in HzRGs because of inverse Compton losses, which are due to a denser CMB that affect the higher frequencies, resulting in a steeper high-frequency spectral index. Also present are free-free or synchrotron self-absorption, due to the compact sizes of radio sources at high-redshifts which can lead to a turnover in the low frequency spectrum (Saxena et al., 2018b).

The segments from mid-to-far infrared through to submillimetre wavelengths are dominated by thermal dust emission, which is heated by the AGN and star formation activity (Seymour et al. 2008). Seymour et al. (2008) found a possible association between star formation at high-redshift and powerful, obscured AGN.

X-ray observations of HzRGs can be used to trace hot ionised gas, heated by X-rays from the AGN or UV photons from young stars. Non-thermal emission from inverse Compton scattering is also detectable in X-rays. Submillimetre luminosity increases with redshift, with a $(1 + z)^3$

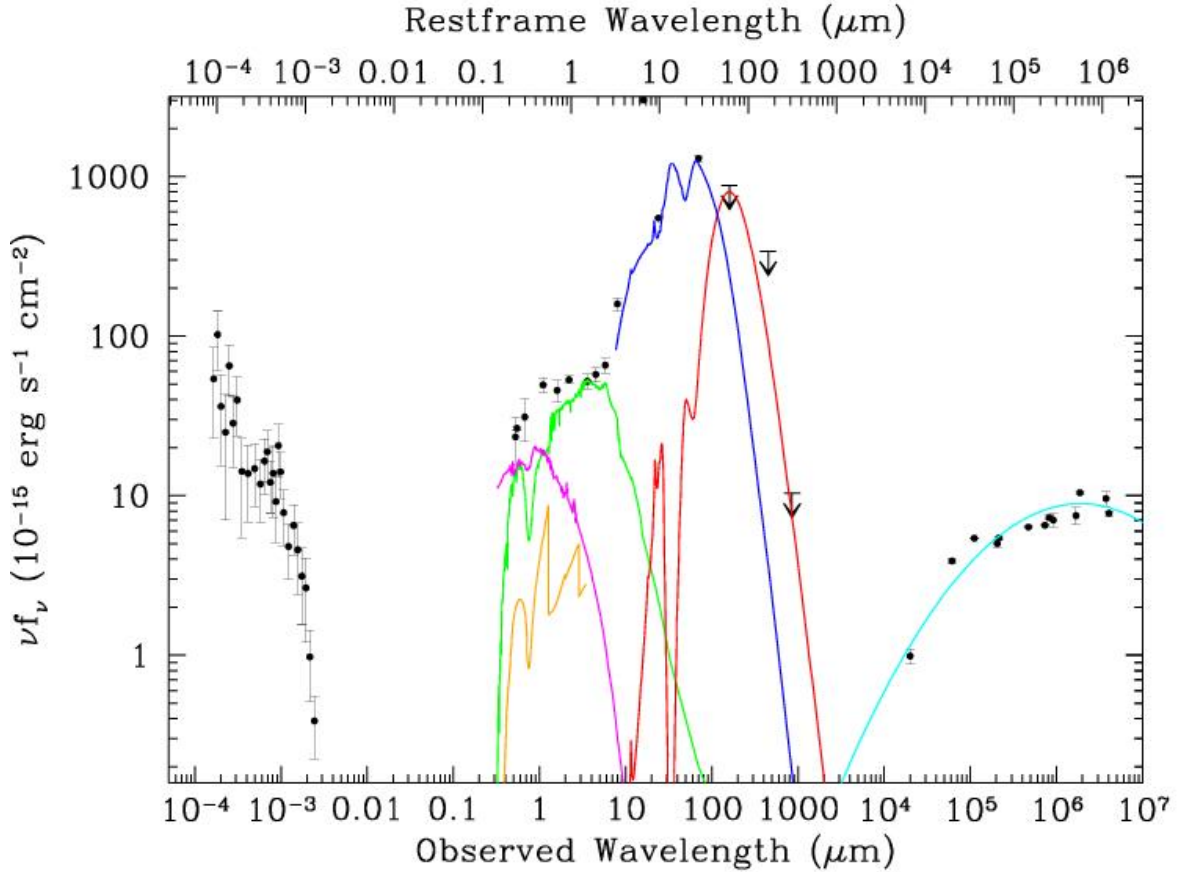


Figure 2.6: Panchromatic view of spectral energy distribution of high-redshift radio galaxy 4C 23.56, $z = 2.5$. The spectra has been decomposed into its various components: *Cyan*: radio synchrotron; *Black*: Absorbed non-thermal X-Ray AGN; *Yellow*: nebular continuum; *Blue*: AGN-heated thermal dust emission; *Red*: Starburst-heated dust emission; *Green*: stars; *Magenta*: scattered quasar (Miley and De Breuck, 2008).

dependence out to $z \sim 4$, implying that star formation rates were higher and that quasars were brighter in HzRGs at $z > 3$ (Miley and De Breuck, 2008).

When redshift is plotted against the spectral index of HzRGs, there appears to be a loose relationship, dubbed the $z - \alpha$ relation. It is thought that this may be due to radio sources at high redshift doing extra work against a denser medium, which would lead to less adiabatic expansion losses and therefore more synchrotron losses, resulting in a brighter source with a spectrum that steepens faster (Ker et al., 2012). However, Miley and De Breuck (2008) speculate that the $z - \alpha$ relation may be an indirect manifestation of a separate Luminosity - α effect (which may be a reflection of unintentional sample bias).

One curious subset of infrared radio sources is infrared-faint radio sources (IFRS), which have flux densities of several mJy at 1.4 GHz, but are very faint in infra-red wavelengths (Middelberg et al., 2011). Infrared-faint radio sources can be classified as AGN from their radio luminosities, although they are less luminous but more abundant than high-redshift radio galaxies (Middelberg et al., 2011). They probably represent obscured radio-loud AGN which have not been previously studied, and brighter IFRS will likely be very similar to HzRGs.

2.4 K - z relation

One of the key characteristics of high-redshift radio galaxies is the K - z relation, also known as the Hubble K - z diagram. This phenomena was first identified by Lilly and Longair (1984), who found that infrared wavelengths, even at $z \sim 1$, were dominated by stars on the Giant Branch

of the Hertzsprung-Russell diagram.

When examined in near-infrared (K -band) wavelengths ($2.2 \mu\text{m}$), the luminosities of local ($z \sim 0$) ellipticals are dominated by the bulk of old, low mass red stars, with little star formation activity, suggesting that intense periods of star formation must have occurred at some point in their past. At higher redshifts, the K -band emission is due to the redshifted emission of young, blue luminous stars, suggesting these galaxies were more gas-rich and formed stars more readily in the past (Rocca-Volmerange et al. 2004). HzRGs are usually galaxies with the largest K -band luminosities in the early Universe (Miley and De Breuck, 2008). Rest-frame near-infrared (NIR) studies are also valuable for probing galaxy stellar masses (Seymour et al., 2007).

While useful, K -band photometry can be contaminated by warm dust components which must be appropriately accounted for, and K -band flux can be contaminated by strong emission lines at certain wavelengths, leading to an overestimation of stellar mass. Seymour et al. (2007) found that once contaminants had been accounted for, a majority of HzRGs have stellar masses in the range $10^{10} - 10^{11} M_{\odot}$, even at redshifts of $z \sim 4$, placing radio galaxies at the extreme end of galaxy stellar mass functions.

A study of deep NIR HzRG images by van Breugel et al. (1998) found good correlation with the K - z relationship, suggesting that rest-frame optical light from these objects is dominated by stellar populations evolving passively from their formation epoch at $z > 5$. Their study also found that radio galaxies at $z > 3$ evolve into much larger elliptical systems than radio-quiet galaxies and are consistent with models where such galaxies form in a hierarchical fashion, through mergers with smaller star-forming systems (van Breugel et al., 1998).

One problem noted by van Breugel et al. (1998) was that if $z > 3$ HzRGs are indeed the progenitors of massive ellipticals with $M_* = 10^{12} M_{\odot}$, than this would stand at odds with contemporary cosmology formation models, where such large systems were thought to form relatively later (ie. at lower redshifts/less distant).

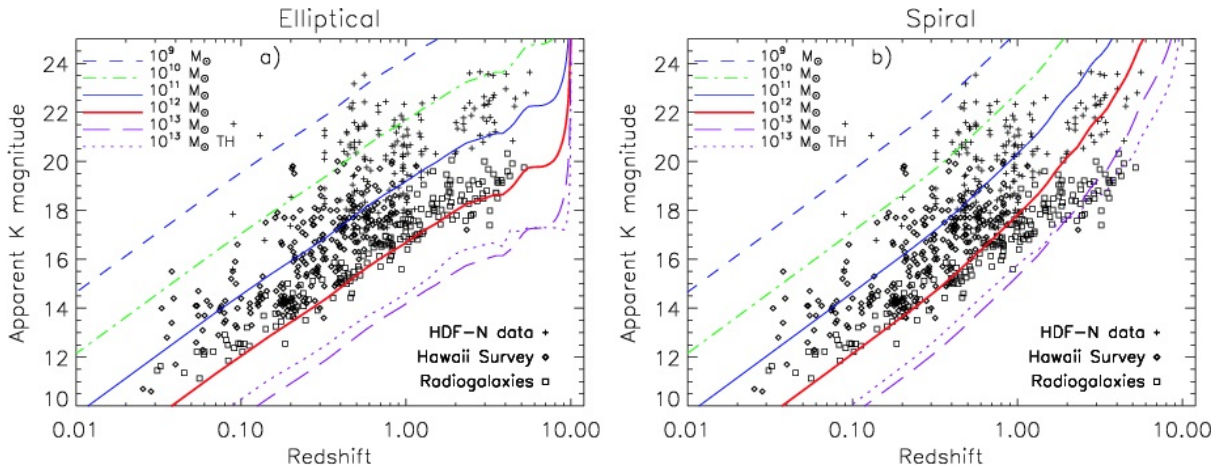


Figure 2.7: K -band sequences for elliptical and spiral galaxies, plotted against models of galaxy mass functions generated by the PEGASE.2 galaxy evolution simulation (Rocca-Volmerange et al., 2004).

Rocca-Volmerange et al. (2004) found that the K - z relation is due to a galaxy mass limit of $10^{12} M_{\odot}$. Using the PEGASE.2 galaxy evolution simulation (Fioc and Rocca-Volmerange, 1999) they found that, in contrast with spiral galaxies, the maximum mass an elliptical galaxy would attain was $10^{12} M_{\odot}$ (see Figure 2.7). At higher redshifts, galaxy evolution effects become dominant when star formation rates were more intense, particularly when z -formation values are high (which was $z = 10$ in Rocca-Volmerange et al. 2004). The term z -formation refers to the epoch in which infall and initial star formation began, when the galaxies took shape and began to form stars.

As Rocca-Volmerange et al. (2004) point out, since the K - z relation applies to the most luminous radio galaxies, this implies the presence of the most massive black holes. These results would mean that massive elliptical galaxies were formed from the accumulation of mass on a very short time scale. This is intimately tied to SMBH formation and implies a dependence on the star formation process.

Their findings appear to have been confirmed by later research. Seymour et al. (2007) surveyed 69 radio galaxies with $1 < z < 5.2$ at infrared wavelengths and found radio galaxies have stellar masses mostly within the $10^{11} - 10^{12} M_{\odot}$ range, with almost no dependence on redshift and a scatter of less than 50 per cent. The small scatter suggests that the observed K - z relation at $z > 1$ is due to the intrinsic homogeneity of the HzRG population (Seymour et al., 2007). This implies an early formation epoch for these massive galaxies (De Breuck et al. 2010). In their survey of 32 HzRGs, Saxena et al. (2019a) found the $10^{12} M_{\odot}$ limit stood in their sample as well. In addition, several extremely red objects in the 7C survey had inferred ages of a few Gyr, implying that they formed the bulk of their mass at $z \sim 5$ (Jarvis et al. 2001).

A study by De Breuck et al. (2010) found that stellar masses of HzRGs have low scatter around $\sim 2 \times 10^{11} M_{\odot}$. They found a small dip in stellar mass around $z = 3$, possibly suggesting that the bulk of stellar populations had already been built by this epoch, implying higher star formation rates at $z > 3$. Low stellar mass spread suggests that radio power, stellar mass or both are not strongly correlated with the accretion properties of the central SMBH (De Breuck et al., 2010).

2.5 Luminosity at high redshifts

There is likely a relationship between the K -band brightness and radio luminosity of radio galaxies. Dunlop and Peacock (1993) found that the K -band structures of 3C radio galaxies aligned closely with radio axes at $z \sim 1$, but the K -band structures of other faint sources at similar magnitudes are not aligned with radio axes, suggesting to them that the radio-optical alignment was related to radio luminosity rather than redshift. Many HzRGs have gas masses comparable to gas-rich spiral galaxies, inferring star formation rates that in our local Universe are rivalled only by galaxy-galaxy mergers. Eales et al. (1997) found that the NIR light from 3C radio galaxies at $z \sim 1$ is dominated by non-stellar light, while NIR light from 6C/B2 HzRGs (which are generally more distant) is dominated by stellar light.

The luminosity and power of an HzRG depends on the morphology, density and inhomogeneity of the gaseous protogalactic medium, as well as the age and duty cycle of the radio source (van Breugel et al., 1998). Radio luminosity is intrinsically tied to black hole mass and accretion rates. The maximum possible luminosity of a SMBH is the Eddington Luminosity, and the Eddington ratio (from 0 to 1) indicates how effectively the black hole is accreting, by comparing the bolometric luminosity to the Eddington luminosity, L_{bol}/L_{Edd} (Saxena et al., 2018b). The most core-dominated radio galaxies are also the most luminous hot dust emitters (De Breuck et al. 2010) and generally, since the mass of a SMBH sets the Eddington limit, this means massive black holes are more luminous and easier to detect (Padovani et al. 2017).

Ker et al. (2012) found that radio sources at high redshift are increasingly likely to be young and small, because radio sources fade as they grow in size due to decreasing ambient density. This means that only radio sources that are young and radio-bright are selected by the popular Ultra-Steep-Spectra method (see Section 2.7), something that Blundell and Rawlings (1999) have termed the ‘youth-redshift degeneracy’, making older radio galaxies at high- z difficult to detect. The youth-redshift degeneracy is most obvious over a luminosity range with a steep luminosity function.

The extreme power generated by jets places limits on the epoch of radio galaxy formation and growth, with further limits placed by the Eddington limit of accreting SMBHs (Blundell and Rawlings, 1999). In their article on HzRG luminosity, Saxena et al. (2018b) modelled luminosity of radio galaxies at $z = 6$, concluding that in order for SMBHs to be large enough to power luminosities of the order required to classify as radio loud this distance (ie. $L_{500} > 10^{28}$ W Hz $^{-1}$), they must have been accreting at close to their Eddington limits from their very early formation, and be maximally spun up. They note that any HzRG at $z = 6$ must be very young, compact and lose energy at a rate much higher than that seen at lower redshifts. This concurs with the youth-redshift degeneracy of Blundell and Rawlings (1999).

2.6 Previous Surveys

The main surveys of relevance to this project are the Third Cambridge (3C) and Sixth Cambridge (6C) surveys.

The Revised Third Cambridge (3CR) radio survey was carried out at frequencies of 38, 178, 750, 1400, 2695, and 5000 MHz, with $S_{178} > 9$ Jy. Data from this survey was used to identify 85 radio galaxies (Kellermann, Pauliny-Toth and Williams 1969; Lilly and Longair 1984). The median redshifts of the 3CR galaxies and quasars are 0.27 and 0.91 respectively, with a median z for FR II radio galaxies of 0.422. Approximately 16 percent of radio galaxies lie at $z > 1$, with one $z > 2$ (McCarthy 1993). Hosts of 3C radio galaxies at $z \sim 1$ are consistent with massive elliptical galaxies, whose infrared emission is dominated by starlight from old red stars (Jarvis et al. 2001).

The 3C survey was flux limited, so radio luminosity and redshift are tightly correlated, meaning that the most distant sources are also the most luminous, which in turn produce the strongest emission lines. This means that any observed differences between low and high-redshift radio galaxies may be attributable as much to differences in luminosity as to redshift (Eales et al. 1997).

The 6C sample was a filtered sample, using steep spectra ($\alpha \geq 0.981$) and small angular size ($\leq 15''$) to identify candidates for redshift measurement (Allington-Smith 1982; Eales et al. 1985; Jarvis et al. 2001). The 6C dataset is comprised of the 408 MHz B2 survey and the 151 MHz 6C survey. Both have radio flux limits about 6 times fainter than 3C, with B2 flux limits from 1 Jy to 2 Jy at S_{408} and 6C flux limits from 2.2 to 4.4 Jy at S_{151} . 3C galaxies were in general more luminous than the less radio-powerful 6C sources (Rocca-Volmerange et al. 2004). Jarvis et al. (2001) sampled the 6C dataset to obtain 29 spectra, 12 of which lay at $z > 2$. The flux density at 151 MHz was in the range 0.96 - 2 Jy.

2.6.1 Demographic summary of HzRGs

Radio galaxies are almost non-existent at low redshifts, with the density of steep spectrum radio sources decreasing by a factor of 100-1000 between $0 \leq z < 2.5$. Dunlop and Peacock (1990) observed a rise in the density of HzRGs (compared to other galaxies in the local Universe) around $z \sim 2$, with a density decline between $z = 2$ and $z = 4$ (see also Jarvis et al. 2001). However, Miley and De Breuck (2008) note the presence of a 'redshift desert' at $1.2 < z < 1.8$, where the [OII] $\lambda 3727\text{\AA}$ is too red and the Ly α $\lambda 1216\text{\AA}$ is too blue to be easily observed from ground based telescopes. This had led to an under representation of HzRGs at these distances, and a skewing of HzRG densities at these distances in comparison to other galaxy types. The density of bright radio sources in the redshift range $2 < z < 5$ is a few times 10^{-8} Mpc $^{-3}$, with a high degree of uncertainty (Jarvis et al., 2001; Miley and De Breuck, 2008).

Some of the challenges affecting identification of HzRGs is the lifespan of their radio sources.

Saxena et al. (2019b) suggest that the primary means of energy loss in HzRGs at $z > 4$ is enhanced inverse Compton losses. This dominates other energy loss mechanisms such as synchrotron or adiabatic losses and means HzRGs are usually only active for between $10^5 - 10^8$ years. Radio-quiet sources and quasars are much shorter lived and may have only been active for a few 100 years (Miley and De Breuck, 2008).

As redshifts increase, the morphology and radio spectrum of the HzRG change. At larger redshifts the typical radio galaxy has an extended appearance (ie. jets and lobes), with radio luminosity increasing, the typical size decreasing and the typical spectra steepening (Miley and De Breuck, 2008). At $z > 3$, radio galaxy morphologies exhibit structures on two different scales: relatively bright, compact components with typical sizes of ~ 10 kpc surrounded by large-scale ($\sim 50\text{-}100$ kpc) faint and diffuse emission. The brightest components are often aligned with radio sources and have individual luminosities comparable to nearby galaxies (van Breugel et al., 1998).

In an analysis of 86 published radio galaxies at $z \geq 2$, Saxena et al. (2019b) found a median angular size of 42 kpc, with a median size of 22kpc from their own survey of 13 radio galaxies. Saxena et al. (2018b) used models to predict the linear sizes of HzRGs at $z = 6$ and found they would have a median size of 20 kpc, translating to roughly 3.5 arcseconds projected angular size on the sky.

A study of van Breugel et al. (1998) found that radio galaxies at $z > 3$ are very blue, consistent with a young stellar population. This suggests a link between star formation activity and radio emission at high redshift, with these two processes likely triggered by the same mechanism (Jarvis et al. 2001). Submillimetre observations found that dust masses in radio galaxies at high redshift were higher than those with similar radio luminosities at lower redshift, implying that star formation rates rose with increasing redshift (Jarvis et al. 2001).

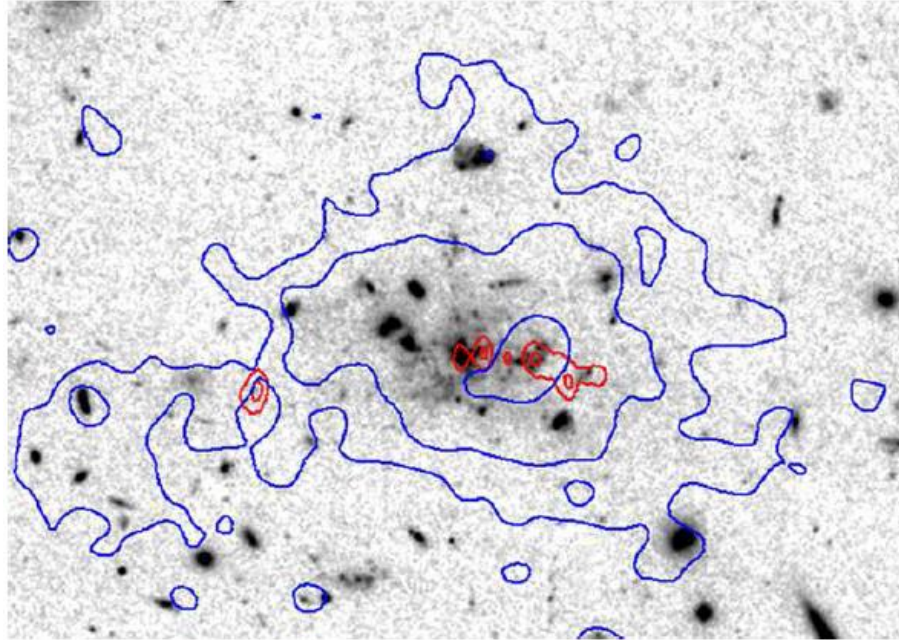


Figure 2.8: Spiderweb galaxy (MRC 1138-262). With a redshift of $z = 2.2$, this large radio galaxy is in the process of merging with numerous satellite galaxies (Miley and De Breuck, 2008). The blue contours are Ly α , with showing a gaseous nebula surrounding the cluster, and the red contours from 8GHz radio data and indicate non-thermal radio emission.

Radio galaxies at low redshifts are often at the centre of massive galaxy clusters. These clusters are crucial to tracing the formation of the most massive dark matter haloes, galaxies and SMBHs. One frequently used example is MRC 1138-262, the 'Spiderweb Galaxy' (Figure 2.8,

where UV and optical imaging shows numerous satellite galaxies orbiting and merging with the central radio galaxy.

Using cross-correlation techniques, Longair and Seldner (1979) found HzRGs to be within over-dense regions. FR I intermediate and lower power sources are found in the highest density environments, often in the cores of rich clusters, with FR II galaxies in less dense environments than rich clusters, but still higher than average galaxy density. FR II sources often show evidence for tidal interactions and merging (McCarthy 1993). Heckman et al. (1985) found radio galaxies were in an environment 2-3 times more dense than radio-quiet ellipticals.

2.7 Common methods of detection and investigation

Most HzRGs have been found using criteria designed to preferentially select high-redshift, high luminosity sources. This has been driven by the practical difficulties of obtaining redshift measurements for faint radio sources, often involving significant amounts of observing time on large optical and infrared telescopes (Eales et al. 1997). A number of selection techniques have been developed to increase the identification rate of HzRGs from large radio surveys. Miley and De Breuck (2008) have reviewed the more common and successful techniques, which are summarised here.

One of the main methods of filtering HzRG's from other radio sources is through use of spectral indices. High redshift radio sources have been found to have ultra-steep spectral indices ($\alpha \leq -1$) (Blumenthal and Miley, 1979; Tielens et al., 1979), so it is now common practice to filter radio sources based on the steepness of their spectral index (Equation 2.1). Spectral indices are typically calculated by taking the flux density at two frequencies, where:

$$\alpha = \frac{\ln(S_\nu/S_0)}{\ln(\nu/\nu_0)} \quad (2.2)$$

This two point spectral index is denoted as $\alpha_{\nu_1}^{\nu_2}$. In this report, both ν_1 and ν_2 are expressed in MHz.

Another method of preferentially filtering high-redshift radio galaxies is to restrict the angular size of the radio source. Miley (1968) first noted that angular size decreased in radio sources with high redshifts. One of the main reasons why radio sources appear smaller at high redshift is the increase in the density of the ambient medium surrounding these galaxies. This increased density makes it more difficult for radio jets to expand to large distances, as they lose more energy thrusting into the denser environment. Moreover, CMB density increases as $\propto(1+z)^4$, leading to increased inverse Compton losses. Combined, these serve to extinguish radio sources while they are still young, leading to an overall decrease in their size.

The next step is to closely match radio sources to optical or infrared data. Using the $K-z$ relation, once a bright K -band counterpart to a radio source has been identified, the radio source may be discarded.

While steep spectral indices are often used as a primary means of filtering HzRG candidates, Ker et al. (2012) found that K -band selection was more efficient than radio-based selection to maximise the number of high redshift sources. They also found that applying steep spectrum criteria alone is not sufficient, as the $z - \alpha$ correlation is strongest for extended radio sources. The very high-redshift radio galaxies have more characteristics of young radio sources, as they are compact in size and still confined within their host galaxies.

The final selection technique discussed here is to observe radio galaxy candidates at various wavelengths, to obtain spectroscopic redshift measurements and measure their star formation rates and interactions with their environments. To begin, deep K -band imaging is used to

identify the host galaxy and obtain an accurate position. Once this position has been obtained, a long-slit spectroscope can be placed at this location. Since individual radio telescopes operate over a limited range of frequencies, to characterise the broadband spectrum requires combination of data from a wide range of telescopes observing across the EM spectrum (Kellermann and Owen 1988). In addition to optical spectroscopy, radio interferometers like the Atacama Large Millimeter/submillimeter Array (ALMA) are precise enough that they can be used to detect molecular line transitions and thus determine redshift.

Radio galaxies have rich emission-line spectra. Classical radio galaxies have spectra with narrow permitted lines ($\text{FWHM} < 2000 \text{ km/s}$) and strong forbidden lines, while quasars have broad permitted lines and relatively weak forbidden lines (McCarthy 1993). The primary emission line used for redshift measurement is $\text{Ly}\alpha 1216\text{\AA}$, with other useful lines being CIV $\lambda 1549\text{\AA}$, HeII $\lambda 1640\text{\AA}$ and CIII] $\lambda 1909\text{\AA}$ (Miley and De Breuck, 2008). The first detection of $\text{Ly}\alpha$ in high redshift galaxies were made by Spinrad et al. (1985) in galaxies at redshift $z > 1.8$.

The 'Lyman break' selection technique may be useful at very high redshifts ($z \geq 3$), when the rest frame ultraviolet light has redshifted into optical wavelengths. This is due to a 'break' in the spectrum of a star forming galaxy produced by the absorption of radiation by neutral gas that surrounds the stars at wavelengths blueward of the Lyman limit (912 Å). However, this relies on very deep photometry in multiple optical bands and is not practical for large radio surveys with potentially hundreds of candidates over thousands of square degrees of sky.

2.7.1 Case studies: TN J0924-2201 and TGSS J1530+1049

This section examines the methods behind the identification of two of the most distant radio galaxies, TN J0924-2201 and TGSS J1530+1049. Both made use of the methods described above and are good examples of commonly accepted methods for detecting high-redshift radio galaxies.

TN J0924-2201

For nearly two decades, the most distant radio galaxy was TN J0924-2201, with $z = 5.19$ (van Breugel et al., 1999). It was selected as part of a sample of 'ultrasteep' spectrum sources, with $\alpha_{1400}^{365} < -1.30$ and $S_{1400} > 10 \text{ mJy}$ (De Breuck et al., 2000).

Radio observations found TN J0924-2201 had a spectral index of $\alpha_{1400}^{365} = -1.63 \pm 0.08$, among the steepest in the whole sample, with a flux density $S_{1400} = 73.3 \pm 1.5 \text{ mJy}$ (De Breuck et al., 2000).

After spectral identification, van Breugel et al. (1999) used the Near Infrared Camera at the Keck I telescope to conduct K -band observations and estimated the source to have a K -band magnitude of $K = 21.3 \pm 0.3$. Spectrographic observations followed on the Low-Resolution Imaging Spectrograph at the Keck II telescope, showing a single emission line at $\lambda \sim 7530 \text{ \AA}$, which the researchers interpreted as $\text{Ly}\alpha$, giving the radio galaxy a redshift of $z = 5.19$ (van Breugel et al., 1999).

TN J0924-2201 has a very small radio size (8 kpc), indicating it is a relatively young radio galaxy, and/or embedded in an overdense environment. For comparison, the three next distant radio galaxies at the time, with redshifts of 4.41, 4.25 and 4.11 have radio sizes of 19, 28 and 37 kpc respectively.

TGSS J1530+1049

The most distant radio galaxy currently known is TGSS J1530+1049, reported by Saxena et al. (2018a) with a redshift of $z = 5.72$. This galaxy was selected from data in the TIFR GMRT Sky Survey (TGSS) (Intema et al. 2017), which surveyed the entire radio sky north of Dec -53 at

150 MHz. Saxena et al. (2018a) shortlisted the TGSS sample to 588 candidates with compact morphologies, $S_{150} < 0.4$ Jy and ultra-steep spectra ($\alpha_{1400}^{150} = -1.3$). TGSS sources were cross-matched with the VLA FIRST survey at 1.4 GHz to calculate the steepness of their spectral index. Compact morphologies (largest angular size $< 10''$) helped limit candidates to high redshift sources, resulting in a final sample set of 32 radio sources (Saxena et al. 2019a).

To maximise the chances of selecting a high-redshift source, infrared and optical comparisons were made to filter out radio sources that appeared in these wavelengths. High-resolution radio imaging was done using the Karl G. Jansky Very Large Array (VLA) to obtain morphology and sub-arcsecond positions for spectroscopic followup.

TGSS J1530+1049 has flux densities of $S_{150} = 170 \pm 34$ mJy and $S_{1400} = 7.5 \pm 0.1$ mJy, a spectral index of $\alpha_{1400}^{150} = -1.4 \pm 0.1$ and a compact size of 0.6 ± 0.1 arcsec (Saxena et al., 2018a). Spectrographic and deep K -band imaging were done next, with a K -band magnitude of 22.4 and a single emission line at 8170 Å. This emission line was interpreted as Ly α , providing TGSS J1530+1049 with a redshift of $z = 5.72$. This high redshift was seemingly supported by the K -band magnitude via the K - z relation.

Using this redshift data, Saxena et al (2018a) calculated that TGSS J1530+1049 has a restframe luminosity of $L_{150} = 10^{29.1}$ W Hz $^{-1}$ and $L_{1400} = 10^{28.2}$ W Hz $^{-1}$, making it one of the more luminous high redshift radio galaxies thus discovered. Saxena et al. (2018a) note however, that while this source was selected for its ultra-steep spectral index, at low frequencies the spectrum flattens out, with $\alpha_{365}^{150} = -0.16$. If these low frequencies had been used in the initial selection phase, TGSS J1530+1049 would not have been shortlisted. Saxena et al. (2018a) suggest that search techniques for HzRGs should consider radio colours instead of a simple USS selection. Radio colours are used to indicate frequency, with red the lowest frequencies and blue the highest. This flattening of spectral index at low frequencies was also noted by Saxena et al. (2018b) in several other sources in their study (10/17 sources).

Chapter 3

Methodology

As seen in the previous chapter, the most common method of detecting HzRGs, via selection of ultra steep spectral index and flux limits, is not ideal. As noted by Saxena et al. (2018a), low frequency flattening of the radio spectra means TGSS J1530+1049 would not have been found if low frequency spectral indices had been used in a survey that depended on an ultra-steep spectral cut. Applying this in a more general fashion, a USS cutoff could result in a significant fraction of distant sources being removed from a sample. Using a small sample of highly complete radio galaxies, Ker et al. (2012) compared spectral index, luminosity, linear size and redshift, concluding that the most effective methods of selecting distant radio sources are based on a combination of criteria, such as near-infrared magnitude and radio spectrum.

3.1 Pilot study

Drouart et al. (2020) devised a new selection technique to identify powerful ($L_{500} > 10^{27}$ W Hz $^{-1}$) radio galaxies at $z \sim 6$, towards the end of the Epoch of Reionisation. The study used data from third internal data release (IDR3) of the Galactic and Extragalactic All-sky Murchison Widefield Array (GLEAM) survey catalogue (Hurley-Walker et al., 2017), with sources detected in broad-band low resolution (~ 2 arcmin) images across 170-230 MHz, with data for the survey taken from 72-231 MHz. GLEAM is useful for HzRG surveys because it provides spectral information over a wide bandwidth: Flux densities were obtained using twenty 8 MHz subbands with prioritised positions, allowing a low frequency spectral energy distribution to be constructed.

This is advantageous to HzRG studies because it allows selection based on the actual shape of the low-frequency SED, rather than relying on a single spectral index (which as we have seen above, can flatten or steepen at low frequencies), or trying to interpolate flux densities at different frequencies taken from multiple telescopes, with inherent issues associated with mixing telescope configurations.

Data from GLEAM IDR3 was cross-matched with the NRAO VLA Sky Survey (NVSS) (Condon et al. 1998), using a cross-matching radius of $30''$. Next, Drouart et al. (2020) applied a radio flux density cut of $0.4 \text{ Jy} < S_{151} < 1.0 \text{ Jy}$, in order to remove any bright sources that would likely be low redshift and to preferentially select only the most powerful HzRGs at $z > 5$. This was also performed to maintain a sufficient signal-to-noise ratio within the GLEAM SED.

Using the SED created from GLEAM data, a second-degree polynomial fit in log space was performed, with:

$$\log(S_\nu) = \alpha \log\left(\frac{\nu_{\text{GLEAM}}}{\nu_{151}}\right) + \beta \log\left(\frac{\nu_{\text{GLEAM}}}{\nu_{151}}\right)^2 + \gamma \quad (3.1)$$

Table 3.1: Selection criteria. (Note: ¹ ELAIS S1 too far south for DR2; ² This study)

Field	Equatorial (DR1)	SGP (DR2)	DDT (DR2)	ES1
In VIKING/DDT	7,733	15,393	599 All	215
With single NVSS $\leq 50''$ (from MWA position)	7298	14344	361 ¹	
With single TGSS $\leq 40''$ (from NVSS position)	4482	7464	240	129
With single FIRST $\leq 10''$ (from TGSS position)	3348	n/a	n/a	
Curved with MWA ($N_{\text{CL}} > -1.4$, $\tilde{\chi}^2 < 5$, $ \beta /d(\beta) > 1$)	1195	3225	127	58
$\alpha \leq -0.7$ AND $\beta \leq -0.3\alpha$	420	645	38	30
No AllWISE $\leq 1''$ (FIRST or TGSS position)	164	275		
Plus $\beta \leq -0.3$	163	248		
No AllWISE $\leq 1''$ AND no unWISE $\leq 1''$ (FIRST or TGSS position)	130	243		35
No counterpart in VIKING (visual inspection) ²	45	56		

with ν_{GLEAM} the corresponding central frequency, ν_{151} the central frequency of the total GLEAM frequency coverage (151 MHz) and α , β and γ coefficients of the polynomial: α = spectral index and β = spectral curvature. High redshift radio galaxy 8C 1435+635 ($z=4.25$), which had been studied in detail by Seymour et al. (2007), was used to predict the α and β values at higher redshift. This was then used to establish further selection criteria of $\alpha \leq -0.7$ and $-1.0 < \beta < -0.4$. Further criteria of $\tilde{\chi}^2 < 5$, $|\beta|/d(\beta) > 1$ were applied to ensure robust fitting.

As this was intended as a pilot survey, the GAMA-09 (Driver et al., 2009) survey field was used to spatially restrict the remaining candidates. After filtering candidates to only those within this GAMA-09 field, 52 candidates were remaining (from 2338). These were then visually inspected using VIKING imaging, removing sources that were not very faint or had no NIR counterparts, resulting in 4 candidates for spectroscopic followup.

Deep K -band imaging with the HAWK-I instrument on the Very Large Telescope (VLT) was used to confirm the location of each host galaxy. Australian Telescope Compact Array (ATCA) continuum imaging was done at 5.5, 9.0, 17 and 19 GHz to complete the radio SED coverage. Then ALMA Band 3 spectral scans were done to identify the host galaxy in the HAWK-I images and obtain a redshift via molecular emission lines. At $z > 5$, it was expected that two or more lines of CO would be observed in the full frequency range (Drouart et al., 2020).

Drouart et al. (2020) obtained redshifts of $1.219 < z < 5.55$ for their four candidates, with one source possibly at a redshift of 10.15, although it requires further confirmation. With a redshift of $z = 5.55$, the pilot study had identified the second most distant radio galaxy, with a success rate of 25% and possibly 50%.

3.2 Improvements applied to current study

Following on from the success of Drouart et al. (2020), researchers at CIRA began to use the same selection techniques to select HzRG candidates from a wider survey area and over a larger flux density range. The new study would draw from the updated Galactic and Extragalactic All-sky Murchison Widefield Array survey catalogue (Southern Galactic Pole region: MWA GLEAM Year 1 + Year 2; Franzen et al. in prep.; Equatorial region: Hurley-Walker et al. 2017) and be defined over ~ 1500 square degrees, with two strips centred on Dec 0° and -32° .

While the pilot study had a flux density of $0.4 \text{ Jy} < S_{151} < 1.0 \text{ Jy}$, the new sample would have a flux cut of $S_{151} > 0.04 \text{ Jy}$, an order of magnitude fainter than Drouart et al. (2020), to increase the potential of finding objects with luminosities similar to those of Saxena et al. (2018a), in addition to more powerful HzRGs.

The selection criteria applied to the new study are summarised in Table 3.1. As with the

pilot study, the GLEAM data was used to construct low frequency SEDs, with a second-degree polynomial fit applied (see Equation 3.1). To filter for high redshift sources, criteria of $\alpha \leq -0.7$ and $\beta \leq -0.3\alpha - 0.51$ were applied to the sample spectra. These values are very similar to those of Drouart et al. (2020), but the β values are wider.

After spectral curvature and flux cuts have been applied, the next step is to visually inspect near-infrared imaging from the VISTA Kilo-degree Infrared Galaxy Survey (VIKING) (Edge et al., 2013). At K -band, the VIKING survey imaging is at a wavelength of $2.15 \mu\text{m}$ and has a limiting magnitude of 21.2 [AB]. As this part of the study forms a major component of this semester’s research project, further detail will be provided in the next section.

Following identification and selection of candidates with no infrared/optical counterpart, the next steps will require followup by high resolution infrared and radio telescopes, including HAWK-I, GMRT, ASKAP, ATCA and VLBI for imaging, SED modelling and morphology. Observing time on the ALMA (imaging and spectroscopy) and MWA (HI absorption) instruments is also planned, as is LOFAR 30-80 MHz observations of equatorial data (if technically feasible).

Further analysis of the radio sources may involve examination of broadband polarisation, to investigate whether there is a correlation between Faraday rotation measures and redshift; and investigating the use of interplanetary scintillation as a selection technique for compact sources.

At the start of Semester 1 2020, the research project commenced with 408 radio galaxy candidates. These had been selected after application of the selection criteria described above. The next stage in preferentially selecting HzRG candidates was to visually inspect NIR imaging and remove sources with visible infrared counterparts.

3.3 Data sources and Analysis methods

3.3.1 Data sources

Because the GLEAM resolution was relatively low ($2'-6'$) and to ensure effective crossmatching of radio-infrared sources, radio imaging of GLEAM candidates was obtained from higher resolution radio surveys to ensure that infrared sources were correctly matched with radio counterparts. To provide secondary confirmation of the morphology and characteristics of each source, a second radio image of the candidates was also used, when possible.

Table 3.2: Radio and Infrared Survey data used to identify infrared counterparts of radio sources. VLASS and VIKING datasets were used for each comparison, with the secondary radio source varying in accordance with survey coverage.

Survey Field	Infrared	Radio			VLASS
	VIKING	ASKAP	FIRST	GLASS	
G1 EQU (GAMA)	x		x		x
G1 EQU (not GAMA)	x		x		x
G2 SGP GAMA	x	x		x	x

Table 3.2 lists the datasets used to analyse the three main survey regions: G1 Equatorial (in the GAMA fields), G1 Equatorial (outside of the GAMA fields) and G2 Southern Galactic Pole (in GAMA fields). Radio sources were also examined in the G2 Southern Galactic Pole outside of the GAMA fields by CIRA researchers, but were not done as a part of this study and are not included here.

Radio survey datasets include the Karl G. Jansky Very Large Array Sky Survey (VLASS), which has an angular resolution of $2.5''$ (Lacy et al., 2020); the Faint Images of the Radio Sky at Twenty centimeters (FIRST) survey, with an angular resolution of $5''$ (Becker, White

and Helfand, 1995); data from the Australian SKA Pathfinder telescope (ASKAP) with an angular resolution of 30"; and the GAMA Legacy ATCA Southern Survey (GLASS) at the Australian Telescope Compact Array (Frater, Brooks and Whiteoak, 1992), with a resolution of $\sim 2'' \times 4''$.

3.3.2 Analysis methods

Radio and infrared images were received in Flexible Image Transport System (FITS) format. The astronomical imaging and data visualisation program SAOImage DS9 (DS9; Joye and Mandel, 2003) was used to view the images and manipulate them for comparison.

By manipulating the contrast and scale of the images, it was possible to obtain the clearest picture and identify the presence (or absence) of near-infrared counterparts. To facilitate this, a small script was written in PYTHON to create "region" files for DS9, which overlaid circles on the images, representing angular sizes. Each region was centred on the RA and Dec coordinates of the radio galaxy candidate and consisted of two circles of 5" and 20" radius.

Radio sources within the 5" radius were identified as being "compact", while sources that extended beyond the 5" region were "extended". Radio morphology was identified and recorded for comparison, with most radio sources identified as comprising either a single compact source or multiple components (such as double or triple sources).

3.3.3 Analysing HzRG characteristics

The radio-infrared inspection phase was completed just as the scale of the COVID-19 pandemic began to be revealed, so plans for participation in further investigation of the HzRG candidates were postponed. In response to this, the focus of this project pivoted to evaluation of the physical characteristics of HzRGs, namely the $K-z$ relation, radio-infrared flux ratios and luminosity at different redshifts.

These features were analysed with a sample of 193 radio galaxies from five main surveys/papers. These were:

- 3C: 85 sources (Kellermann, Pauliny-Toth and Williams, 1969; Lilly and Longair 1984)
- 6C: 62 sources (Allington-Smith 1982 and Eales et al. 1985)
- HzRG sample from Miley and De Breuck (2008 review paper): 36 sources (Chambers et al. 1990; De Breuck et al. 2000; De Breuck et al. 2001; De Breuck et al. 2010; Jarvis et al. 2001; Miley and De Breuck 2008; van Breugel et al. 1998)
- Saxena et al., 2019: 7 sources
- Drouart et al., 2020: 3 sources

Radio object MG1131, with an unpublished redshift of $z = 1.1849$ was also included, as it had comparable radio luminosity levels. Where needed, additional source data was obtained from the NASA/IPAC Extragalactic Database (<https://ned.ipac.caltech.edu/>). Flux densities were taken from the listed references or extrapolated using (low frequency) spectral indices.

If the spectral index α was not provided in the literature, it was determined using:

$$\alpha = \frac{\ln(S_\nu/S_0)}{\ln(\nu/\nu_0)} \quad (3.2)$$

Calculations were made using flux densities at 150 MHz and 1.4 GHz. If the recorded flux densities were not made at these frequencies, then spectral index was used to calculate flux at

frequency ν :

$$S_2 = S_1 \left(\frac{\nu_2}{\nu_1} \right)^\alpha \quad (3.3)$$

In order to calculate observed flux density S , using flux S_0 at redshift z :

$$S = S_0(1 + z)^{1+\alpha} \quad (3.4)$$

Radio luminosity at rest frame frequency ν was calculated as:

$$L_\nu = 4\pi D_L^2 S_\nu (1 + z)^{-(1+\alpha)} \quad (3.5)$$

With D_L the luminosity distance.

The HzRG characteristics listed above were loaded onto plots via MATPLOTLIB (Hunter, 2007), using PYTHON packages ASTROPY (Astropy Collaboration et al., 2013) and NUMPY (Oliphant, 2006).

Chapter 4

Results

4.1 Identifying Near-Infrared Sources

Using the methods outlined in the previous chapter, 165 radio sources were visually inspected alongside corresponding VIKING imaging. Of these sources, 59 were not detected in infrared imaging and 47 were retained for further investigation. See Table 4.1 for a summary.

Table 4.1: Results of visual inspection of radio-infrared imaging.

Survey Field	Radio Sources	Not present in VIKING	For further investigation	Compact Sources	Extended Sources
G1 EQU (GAMA)	40	25	20	23	17
G1 EQU (not GAMA)	90	25	25	59	31
G2 SGP GAMA	35	9	2	8	27
Total	165	59	47	90	75

Detailed information on individual sources, and the results of visual analysis, can be found in the Appendix as Tables A.1, A.2 and A.3.

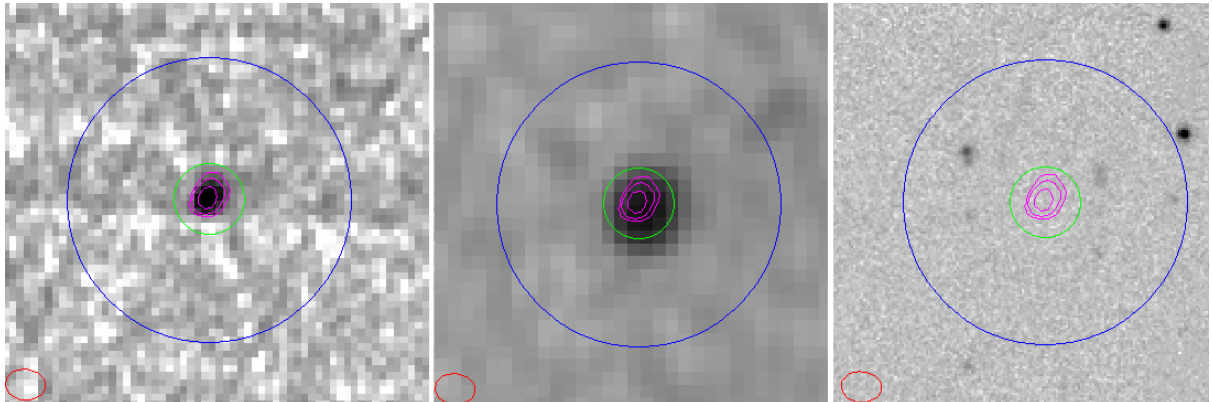


Figure 4.1: GLEAM J090906–010227 (Sources from L-R: VLASS, FIRST, VIKING. Note: Synthesized beam in bottom left-hand corner). Note the lack of infrared counterpart to radio source, shown by overlaying the pink VLASS contours onto the VIKING image (right panel). Selected for further investigation.

Figure 4.1 illustrates an example of a non-detection of an infrared counterpart to a radio source. The higher resolution VLASS image has been used to generate radio contours (seen here in pink), which are then copied across to the VIKING image for inspection and comparison. When the contours are overlaid onto the FIRST image, the difference in angular resolution between the two radio surveys is apparent.

This source is part of the G1 EQU (GAMA) field and, as seen by the pink contour lines in

the right panel, does not have a K -band counterpart. This radio source has been selected as a potential HzRG and will be investigated further.

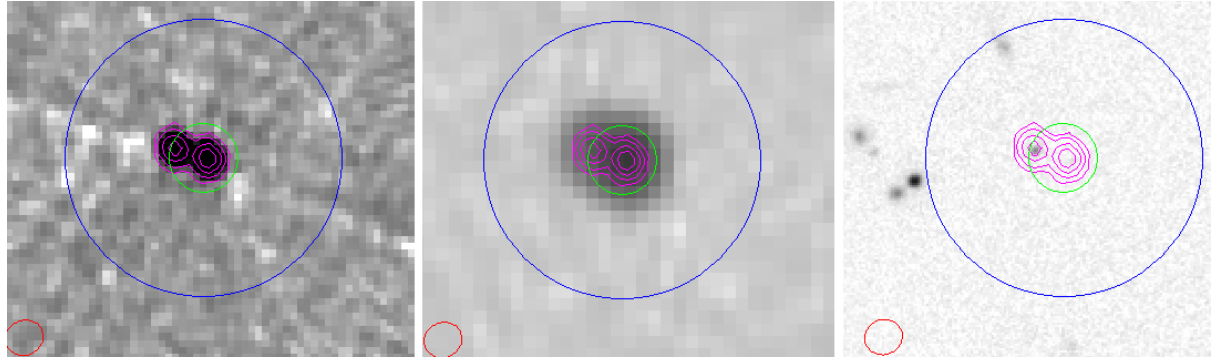


Figure 4.2: GLEAM J092123+013834 (Sources from L-R: VLASS, FIRST, VIKING. Note: Synthesized beam in bottom left-hand corner). Double radio source. Note the presence of a K -band counterpart in the left most contours. Not selected for further investigation.

In contrast, Figure 4.2 provides an example of a double radio source with an infrared counterpart. While faint, the infrared counterpart can be clearly seen in the centre contour of the leftmost radio object. This radio source also extends beyond the $5''$ region and is likely too large to be an HzRG. This object was not selected for further investigation.

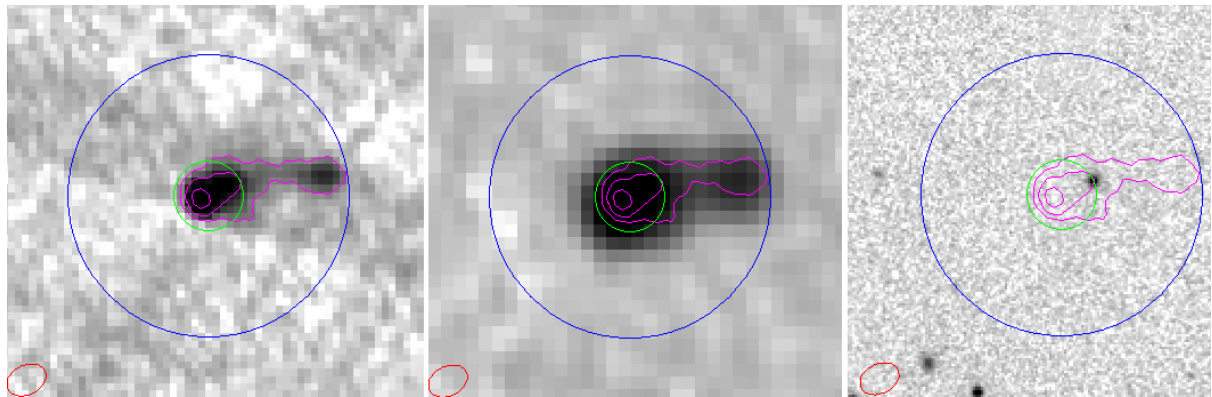


Figure 4.3: GLEAM J114641–000734 (Sources from L-R: VLASS, FIRST, VIKING. Note: Synthesized beam in bottom left-hand corner). Extended/Double radio source. Not selected for further investigation.

Figure 4.3 shows another double source, but with a more extended morphology. The VLASS image (left) shows what appears to be two lobes, with the leftmost lobe brighter, possibly indicative of orientation to observer. The presence of a bright infrared counterpart in the VIKING image is very likely the host galaxy. From visual inspection, this radio source is an FR II (edge brightened) radio source, confirming its identification as a radio galaxy.

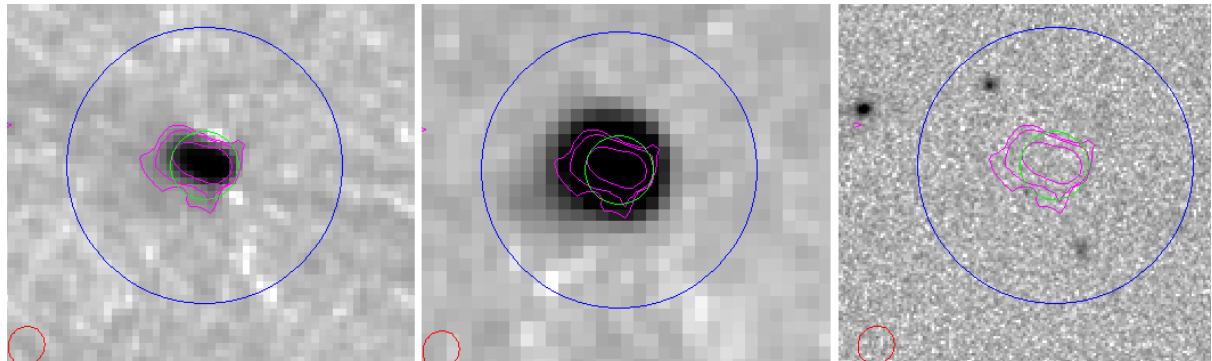


Figure 4.4: GLEAM J143727+014303 (Sources from L-R: VLASS, FIRST, VIKING. Note: Synthesized beam in bottom left-hand corner). Slightly extended radio source with no K -band counterpart. Selected for further investigation.

Figure 4.4 is the last example. It is a slightly extended radio source, as seen by the VLASS image (left), where the contours extend slightly beyond the 5 arcsecond radius in green. Because this radio source is only slightly extended and does not have a K -band counterpart, it has been selected for further investigation.

4.2 HzRG characteristics

This section presents the results of empirical derivations of key HzRG characteristics. See Chapter 5 for discussion of their significance.

4.2.1 $K - z$ Relation

To derive the K - z relation for HzRGs, the K -band magnitude [AB] and redshift from a sample of 193 radio galaxies was plotted using MATPLOTLIB (Hunter, 2007). These are presented in full ($z \geq 0$) in Figure 4.5 and from $z \geq 1$ in Figure 4.6.

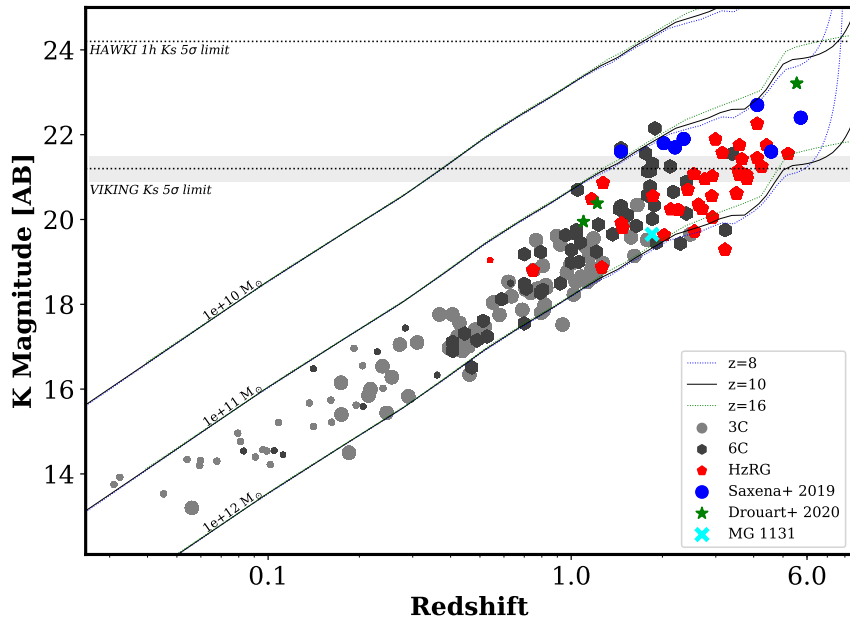


Figure 4.5: K - z relation of a sample of HzRGs (log scale). Markers are sized according to their luminosity, with large markers indicating $L_{500} > 10^{27} \text{ W Hz}^{-1}$. Also plotted are PEGASE.2 K -magnitude tracks for initial galaxy mass functions, at three different formation redshifts.

To illustrate the changes in luminosity at high redshifts, luminosity has been used to trigger marker size, with large markers indicating $L_{500} > 10^{27} \text{ W Hz}^{-1}$.

Also plotted are K -magnitude tracks for elliptical galaxies formed from various initial gas reservoir masses, with different formation redshifts: $z = 8$ (0.641 Gyr); $z = 10$ (0.474 Gyr) and $z = 16$ (0.246 Gyr). These tracks were calculated using the PEGASE.2 galaxy evolution model (Fioc and Rocca-Volmerange, 1999).

To contextualise the visual analysis of radio sources in Section 4.1, the K_s -band 5σ limit of the VIKING survey was included (with uncertainty shaded in grey), as was the K_s 5σ limit of the HAWK-I (ESO) telescope, which will later be used for deep K -band identification of high redshift radio galaxy candidates, prior to spectrographic followup.

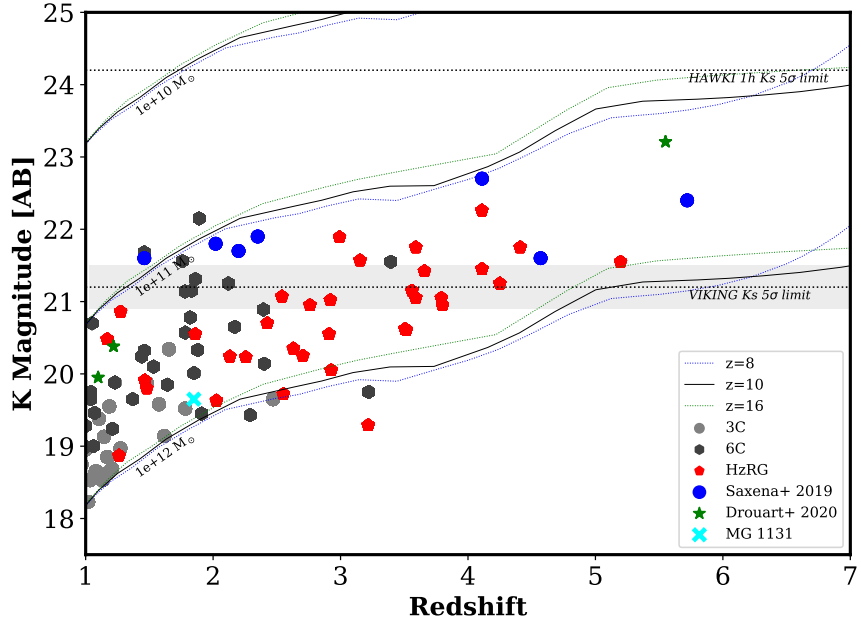


Figure 4.6: K - z relation of a sample of HzRGs, with $z > 1$. Markers are sized according to their luminosity, with large markers indicating $L_{500} > 10^{27} \text{ W Hz}^{-1}$. Also plotted are PEGASE.2 K -magnitude tracks for initial galaxy mass functions, at three different formation redshifts.

4.2.2 Luminosity vs Redshift

The next plot was an examination of luminosity against redshift, presented as $z \geq 0$ (Figure 4.7) and from $z \geq 1$ (Figure 4.8). Marker size was used to indicate spectral index values, with large markers indicating $\alpha < -1.2$. The exceptionally luminous 3C radio galaxy at low redshift is Cygnus A (3C 405), one of the strongest radio sources in the sky and a good analogue for high-redshift radio galaxies.

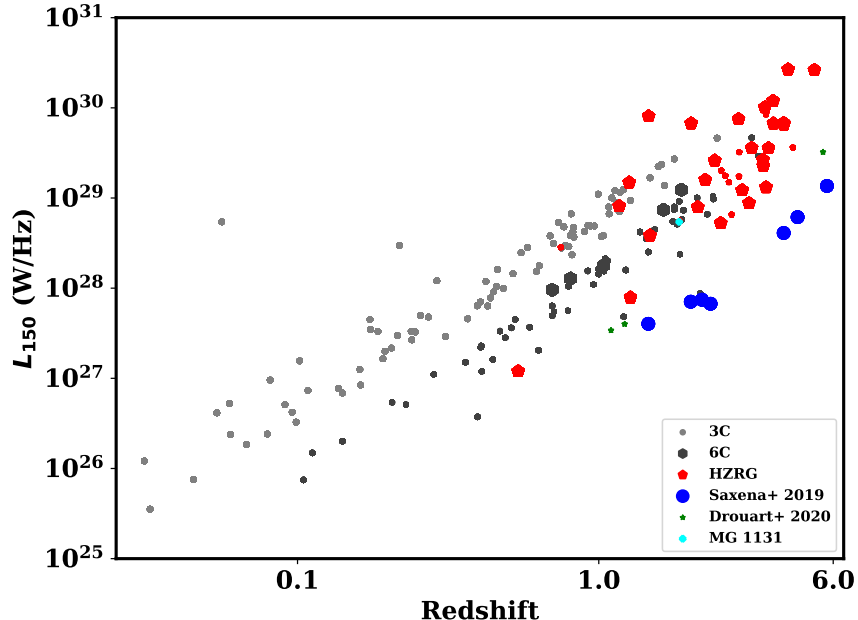


Figure 4.7: Luminosity (L_{150}) vs Redshift (log scale). Markers are sized according to their spectral index, with large markers indicating $\alpha < -1.2$.

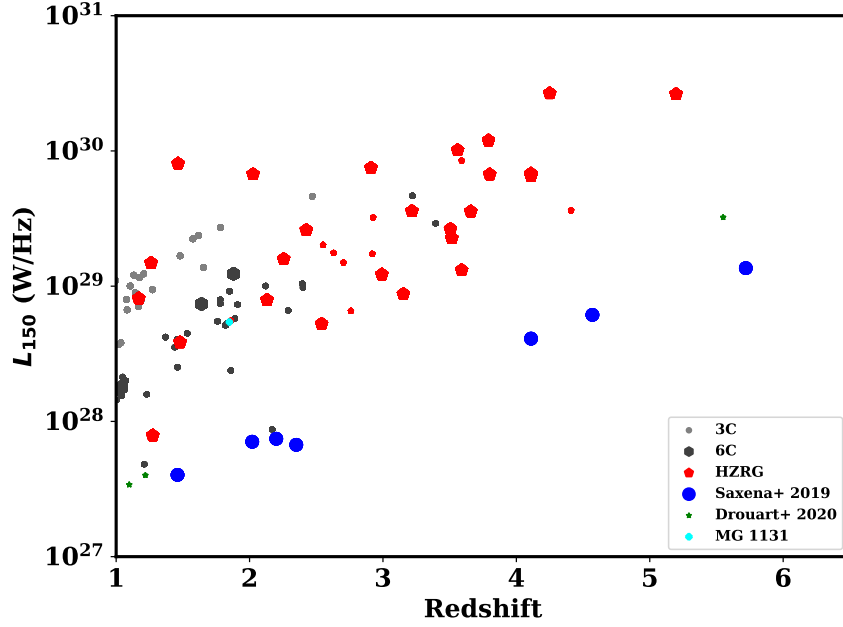


Figure 4.8: Luminosity (L_{150}) vs Redshift, $z > 1$. Markers are sized according to their spectral index, with large markers indicating $\alpha < -1.2$.

4.2.3 Radio K-band Flux Ratios

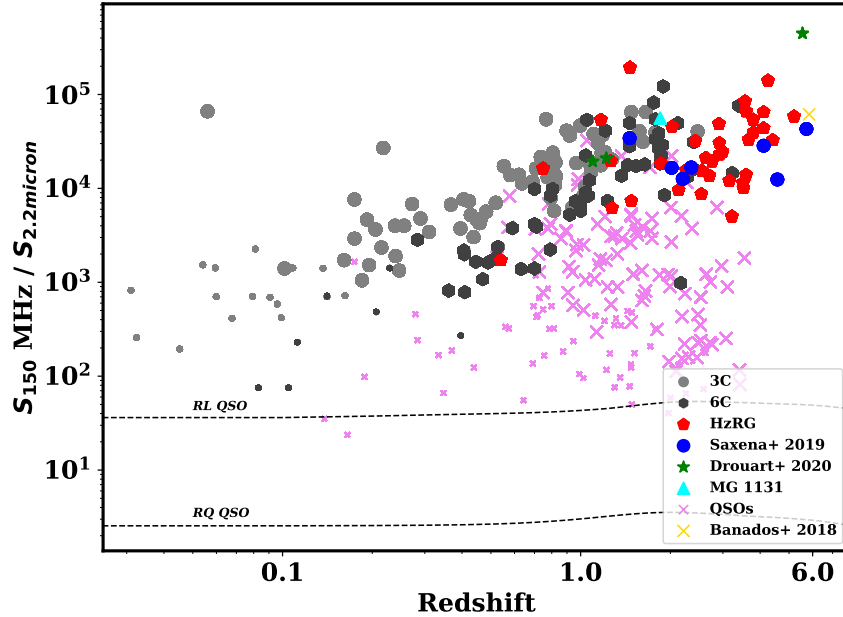


Figure 4.9: K flux ratios at S_{150} , including QSOs. Markers are sized according to their luminosity, with large markers indicating $L_{150} > 10^{27} \text{ W Hz}^{-1}$.

The final HzRG characteristic examined was the ratios of radio (S_{150}) to K -band ($S_{2.2\mu\text{m}}$) flux (Figure 4.9). Marker size was again used to indicate luminosity, with large markers indicating $L_{150} > 10^{27} \text{ W Hz}^{-1}$. K -band magnitude was converted to flux (mJy) by using:

$$S_{2.2\mu\text{m}} = 10^{(26-(Mag+48.6)/2.5)} \quad (4.1)$$

To compare the flux ratios of HzRGs with high redshift quasars, QSOs from the Sloan Digital Sky Survey Quasar Catalog (Paris et al., 2018) were imported into the figure. The radio-loud quasar PSO J352.4034–15.3373 at $z = 5.84$ (Bañados et al., 2018) was also imported, as it has a comparable redshift to the most distant radio galaxies. Ratio lines for radio loud and radio quiet QSOs (Elvis et al. 1994) were added to indicate the radio nature of the QSOs.

Chapter 5

Discussion

5.1 Near-infrared sources

Of the 165 radio galaxy candidates examined in near-infrared as part of this project, 47 were tagged for further investigation. The majority of sources (90/165) examined here had compact morphology and approximately a third (59) had no visible infrared counterpart.

These radio sources are a subset of 408 candidates that had been identified for near-infrared visual inspection, which resulted in 101 galaxies highlighted for further investigation (Equatorial: 45; SGP: 56). The proportion of galaxies highlighted for further investigation as a result of this project are roughly equivalent to the wider project, which is a good indication of the success of the methodology (and its application).

It won't be known whether the study has preferentially selected young distant radio galaxies until redshifts have been obtained. Overall however, the selection techniques employed in this study show promise. When compared to other samples of radio galaxies, such as Saxena et al. (2018a) and Drouart et al. (2020), the K -band limited (> 21.2 mag [AB]) radio objects identified in this report show great promise for being high-redshift candidates. Likewise, limiting the galaxy candidates to compact sources ensures that less distant radio galaxies are filtered out of the shortlist. It is possible to investigate the radio morphologies of these sources further, but would require further observations across a wider range of frequencies, to complete the SED and identify the presence of steep or flat spectrum.

These shortlisted candidates will be reduced further, based on order of priority. Candidates of most interest are those with the lowest K -band rms values, while ensuring a relatively even spread in RA for observation scheduling purposes.

5.2 Characteristics of high-redshift radio galaxies

Through examination of the $K-z$ relation, luminosity-redshift and radio-infrared flux ratios, several of the key characteristics of HzRGs were empirically derived. Overall, this research has highlighted the importance of faint K -band and the radio/ K -band ratio as key selection criteria for identifying high-redshift radio galaxies.

5.2.1 $K - z$ Relation

The $K-z$ relationship (Figures 4.5 and 4.6) clearly shows that the K -band magnitude of radio galaxies increases with redshift. It can be shown that bright radio sources with faint (or no) K -band counterparts are highly likely to be at high redshift.

As indicated by the marker sizes in the figures, distant radio galaxies are highly luminous. But this result also highlights the inherent bias in preferentially selecting brighter galaxies (such as in the 3C and 6C surveys). Later surveys, such as Saxena et al. (2019) and Drouart et al. (2020), have addressed this bias by going deeper and have therefore covered more of the parameter space that was inaccessible to surveys such as 3C or 6C.

The inclusion of the PEGASE.2 galaxy evolution model indicates that radio galaxies are fairly homogeneous, with a tight grouping of stellar masses in the range $10^{11} < M_{\odot} < 10^{12}$. The PEGASE.2 K -magnitude tracks for initial mass functions agree with suggestions that radio galaxies formed early in the history of the Universe as massive, highly luminous objects. This agrees with previous findings by Rocca-Volmerange et al. (2004), Seymour et al. (2007) and Saxena et al. (2019a). The differences between the three z -formation values can best be seen in Figure 4.6 and remains relatively small until $z \sim 5$.

The presence of such massive galaxies in the early Universe has serious implications for galaxy evolution models, especially considering that radio galaxies are powered by supermassive black holes which must have been accreting at high rates not long after their formation. Using the chosen cosmological parameters (see Section 1.2), TGSS J1530+1049 has an age of 0.994 Gyr, which means that if it formed at $z = 10$ (0.474 Gyr), it had very little time to accrue mass and begin accreting at a very high rate. These high rates of accretion are indicated by the high luminosities of radio galaxies, as shown in the luminosity-redshift plots. It is clear that the most luminous radio galaxies must be powered by the most massive black holes, even in the first billion years of the Universe.

5.2.2 Luminosity vs Redshift

From Figures 4.7 and 4.8, there is a clear difference in terms of luminosity between the “HzRG” sample from Miley and De Breuck (2008) and those from Saxena et al. (2019). This is not entirely a surprise, as Saxena’s survey focused on radio sources with lower luminosity and the “HzRG” sample includes radio galaxies that were specifically selected for their luminosity. The current study hopes to find sources that will fill this empty space between the red and blue markers.

The markers in the figure show the majority of high-redshift radio galaxies are dominated by sources with ultra-steep spectral indices, although this is likely also an indication of survey bias and a manifestation of Blundell and Rawlings’ (1999) ‘youth redshift degeneracy’. Note the difference in marker sizes between the sources from Saxena et al. (2019) which relies on ultrasteep spectral indices, and Drouart et al. (2020), which does not rely on an ultra-steep spectral index cut.

Similar to the $K - z$ diagram in Figures 4.5 and 4.6, Figure 4.7 shows a tight correlation, further suggesting that HzRGs are a homogeneous group. There is however more scatter apparent in Figure 4.8 where luminosity values are more dispersed.

5.2.3 Radio K -band Flux Ratios

It can be seen from Figure 4.9 that radio galaxies are highly luminous at radio wavelengths and only the most luminous quasars are comparable, especially at high redshifts. These plots indicate that high-redshift radio galaxies are dominated by synchrotron emission from jets and lobes, in comparison to other radio-loud sources such as QSOs which are dominated by emission from the compact core.

This flux difference can be explained by the AGN unification model (Chapter 2) where, as a result of orientation, the bright outer lobes of quasars are much less bright than the central

component and relativistic jet. In general, only about 10% of radiation from a quasar is emitted at radio wavelengths, with most being emitted at submillimetre wavelengths (Kellermann and Owen 1988). Radio galaxies on the other hand, are highly luminous at the radio wavelengths, as the core is obscured by the dusty torus. This means that radio flux levels are useful in selecting HzRGs.

Chapter 6

Conclusions and Future Work

6.1 Work completed in Semester 1, 2020

In this first semester, 47 HzRG candidates were identified for follow-up as a result of visual inspection of VLASS and VIKING images, using the $K - z$ relation and angular size criteria.

As a result of COVID-19 imposed restrictions, the project shifted emphasis to the empirical derivation of:

- $K - z$ relation
- K -band/radio flux ratios
- Redshift-Luminosity relation

using a sample of 193 radio galaxies. The physical nature of these characteristics was also examined.

6.2 Plans for Semester 2, 2020

This report has detailed work undertaken during the first of two semesters. While some of the planned activities have been altered as a result of the COVID-19 pandemic, there is still opportunity to participate in the ongoing efforts to identify HzRGs at $z > 5$. These include:

- Analysis of ATCA observation data (1/5/2020 and 3/5/2020) of Southern Galactic Pole region candidates
- Using deep K -band images (from HAWK-I or similar surveys) to search for near-infrared counterparts of radio sources
- Expanding the selection criteria to further narrow down HzRG candidates, through analysis of polarisation data and/or interplanetary scintillation
- Further analysis of HzRG characteristics, including 3D plots, to examine the relationship between redshift, flux, luminosity and spectral index.

6.3 Conclusion

By expanding the methodology of Drouart et al.'s (2020) pilot study, this report details participation in an effort to identify radio galaxies at $z > 6.5$, placing these sources firmly in the

Epoch of Reionisation.

If sufficiently bright radio sources can be found at redshifts greater than 6.5, it should be possible to measure absorption signatures of neutral hydrogen and probe the reionisation of the Universe. HzRGs within the Epoch of Reionisation could be used as probes to investigate intermediate or small-scale structures in the neutral IGM, through redshifted HI absorption observations.

Acknowledgements

This scientific work makes use of the Murchison Radio-astronomy Observatory, operated by CSIRO. We acknowledge the Wajarri Yamatji people as the traditional owners of the Observatory site. Support for the operation of the MWA is provided by the Australian Government (NCRIS), under a contract to Curtin University administered by Astronomy Australia Limited. We acknowledge the Pawsey Supercomputing Centre which is supported by the Western Australian and Australian Governments.

Bibliography

- Allington-Smith, J. 1982. “A complete sample of extragalactic radio sources at 1 Jy at 408 MHz — I. The radio observations.” *Monthly Notices of the Royal Astronomical Society* 199:611-631. DOI: 10.1093/mnras/199.3.611.
- Astropy Collaboration et al. 2013. “Astropy: A Community Python Package for Astronomy.” *Astronomy and Astrophysics* 558:A33. DOI: 10.1051/0004-6361/201322068
- Baade, W. and R. Minkowsky. 1954. “Identification of the Radio Sources in Cassiopeia, Cygnus A, and Puppis A.” *The Astrophysical Journal* 119:206-214. DOI: 10.1086/145812.
- Banados, E. et al. 2018. “A Powerful Radio-loud Quasar at the End of Cosmic Reionization.” *The Astrophysical Journal Letters* 861:L14 DOI: <https://doi.org/10.3847/2041-8213/aac511>.
- Becker, R., R. White and D. Helfand. 1995. “The FIRST Survey: Faint Images of the Radio Sky at Twenty Centimeters.” *Astrophysical Journal* 450:559-577. DOI: 10.1086/176166.
- Best, et al. 1998. “HST, radio and infrared observations of 28 3CR radio galaxies at redshift $z \geq 1$ - II. Old stellar populations in central cluster galaxies.” *Monthly Notices of the Royal Astronomical Society* 295:549-567. DOI: 10.1046/j.1365-8711.1998.01245.x.
- Blandford, R. and R. Znajek 1977. “Electromagnetic extraction of energy from Kerr black holes.” *Monthly Notices of the Royal Astronomical Society* 179:433-456. DOI: 10.1093/mnras/179.3.433.
- Blumenthal, G. and G. Miley 1979. “Spectral index dependent properties of steep spectrum radio sources.” *Astronomy and Astrophysics* 80:13-21.
- Blundell, K. and S. Rawlings. 1999. “The Inevitable Youthfulness of Known High-Redshift Radio Galaxies.” *Nature* 399(6734):330-332. DOI: 10.1038/20612.
- Burke, B., F. Graham-smith and P. Wilkinson. 2019. *An Introduction to Radio Astronomy* (4th Edition). Cornwall: Cambridge University Press <https://doi.org/10.1017/9781316987506>
- Carilli, C. and P. Barthel. 1996. “Cygnus A.” *The Astronomy and Astrophysics Review* 7(1): 1-54. DOI: 10.1007/s001590050001
- Chambers, K. et al. 1988. “4C 40.36: A Radio Galaxy at a Redshift of 2.3.” *The Astrophysical Journal Letters* 327:L47-L50. DOI: 10.1086/185137.
- Chambers, K. et al. 1990. “4C 41.17: A Radio Galaxy at a Redshift of 3.8.” *The Astrophysical Journal* 363:21-39. DOI: 10.1086/169316.
- Condon, J. et al. 1998. “The NRAO VLA Sky Survey.” *The Astronomical Journal* 115:1693-1716. DOI: <https://doi.org/10.1086/300337>.
- De Breuck, C. et al. 2000. “A Sample of 669 Ultra Steep Spectrum Radio Sources to Find High-Redshift Radio Galaxies.” *Astronomy and Astrophysics Supplement* 143:303-333. DOI:

10.1051/aas:2000181.

De Breuck,C. et al. 2001. “Spectroscopy of Ultra-steep-Spectrum Radio Sources.” *The Astronomical Journal* 121(3):1241-1265. DOI: 10.1086/319392.

De Breuck, C. et al. 2010. “The Spitzer High Redshift Radio Galaxy Survey.” *The Astrophysical Journal* 725:36-62. DOI: 10.1088/0004-637X/725/1/36.

Driver, S. et al. 2009. “GAMA: towards a physical understanding of galaxy formation.” *Astronomy and Geophysics* 50(5):5.12-5.19. DOI: 10.1111/j.1468-4004.2009.50512.x.

Drouart, G. et al. 2020. “The GLEAMING of the First Supermassive Black Holes”. *Publications of the Astronomical Society of Australia* ???:??

Dunlop, J. and J. Peacock. 1993. “The redshift cut-off in the luminosity function of radio galaxies and quasars.” *Monthly Notices of the Royal Astronomical Society* 247:19-42.

Eales, S. et al. 1985. “A sample of 6C radio sources selected at the peak of the source counts-I.A search for extended sources and multifrequency radio observations.” *Monthly Notices of the Royal Astronomical Society* 217:149-166. DOI: 10.1093/mnras/217.1.149.

Eales, S. et al. 1997. “A first sample of faint radio sources with virtually complete redshifts - I. Infrared images, the Hubble diagram and the alignment effect.” *Monthly Notices of the Royal Astronomical Society* 291:593-615. DOI: 10.1093/mnras/291.4.593.

Edge, A. et al. 2013. “The VISTA Kilo-degree Infrared Galaxy (VIKING) Survey: Bridging the Gap between Low and High Redshift” *The Messenger* 154:32.

Elvis, M. et al. 1994. “Atlas of Quasar Energy Distributions.” *Astrophysical Journal Supplement* 95:1-68. DOI: 10.1086/192093.

Faranoff, B. and J. Riley. 1974. “The morphology of extragalactic radio sources of high and low luminosity.” *Monthly Notices of the Royal Astronomical Society* 167:31P-36P. DOI: 10.1093/mnras/167.1.31P.

Fioc, M. and B. Rocca-Volmerange. 1999. “PEGASE.2, a metallicity-consistent spectral evolution model of galaxies: the documentation and the code”. Eprint: arXiv:astro-ph/9912179.

Frater, Brooks and Whiteoak. 1992. “The Australia Telescope - Overview.” *Journal of Electrical and Electronics Engineering, Australia* 12(2):103-112.

Heckman, T. et al. 1985 “The effect of local galaxy density on the production of powerful radio sources by early-type galaxies.” *The Astrophysical Journal* 288:122-131. DOI: 10.1086/162769.

Hunter J. D. 2007. “Matplotlib: A 2D Graphics Environment.” *Computing In Science and Engineering* 9:90. DOI: 10.1109/MCSE.2007.55

Hurley-Walker, N. et al. 2017. “GaLactic and Extragalactic All-sky Murchison Widefield Array (GLEAM) survey – I. A low-frequency extragalactic catalogue.” *Monthly Notices of the Royal Astronomical Society* 464:1146–1167. DOI: 10.1093/mnras/stw2337.

Intema, H. et al. 2017. “The GMRT 150 MHz all-sky radio survey. First alternative data release TGSS ADR1.” *Astronomy and Astrophysics* 598:A78. DOI: 10.1051/0004-6361/201628536.

Jarvis, M. et al. 2001. “A sample of 6C radio sources designed to find objects at redshift $z > 4$ – III. Imaging and the radio galaxy K-z relation.” *Monthly Notices of the Royal Astronomical Society* 326:1585-1600. DOI: 10.1111/j.1365-2966.2001.04730.x.

Joye, W. and E. Mandel. 2003. “New Features of SAOImage DS9.” *Astronomical Data Analysis Software and Systems XII ASP Conference Series* 295:489.

- Kellermann, K. and F. Owen. 1988. “Radio Galaxies and Quasars”. In G. Verschuur and K. Kellerman (eds) *Galactic and Extragalactic Radio Astronomy* 563-602.
- Kellermann K., I. Pauliny-Toth and P. Williams. 1969. “The Spectra of Radio Sources in the Revised 3c Catalogue.” *The Astrophysical Journal* 157:1-34. DOI: 10.1086/150046.
- Ker, L.M. et al. 2012. “New insights on the $z-\alpha$ correlation from complete radio samples.” *Monthly Notices of the Royal Astronomical Society* 420:2644–2661. DOI: 10.1111/j.1365-2966.2011.20235.x
- Lacy, M. et al. 2020. “The Karl G. Jansky Very Large Array Sky Survey (VLASS): science case and survey design.” *Publications of the Astronomical Society of the Pacific* 132(1009):035001. DOI: 10.1088/1538-3873/ab63eb.
- Lilly, S. and M. Longair. 1984. “Stellar Populations in Distant Radio Galaxies.” *Monthly Notices of the Royal Astronomical Society* 211:833-855. DOI: 10.1093/mnras/211.4.833.
- Longair, M. and M. Seldner. 1979. “The clustering of galaxies about extragalactic radio sources.” *Monthly Notices of the Royal Astronomical Society* 189:433-453. DOI: 10.1093/mnras/189.3.433.
- McCarthy, P.J. 1993. “High Redshift Radio Galaxies.” *Annual Review of Astronomy and Astrophysics* 31:639-88. DOI: <https://doi.org/10.1146/annurev.aa.31.090193.003231>.
- Middleberg, E. et al. 2011. “The radio properties of infrared-faint radio sources.” *Astronomy and Astrophysics* 526:A8. DOI: 10.1051/0004-6361/201014926.
- Miley, G. 1968. “Variation of the Angular Sizes of Quasars with Red-shift.” *Nature* 218(5145):933-934. DOI: 10.1038/218933a0
- Miley, G. and C. De Breuck. 2008. “Distant Radio Galaxies and their Environments.” *Annual Review of Astronomy and Astrophysics* 15:67-144. DOI: 10.1007/s00159-007-0008-z.
- Minkowski, R. 1960. “A New Distant Cluster of Galaxies.” *The Astrophysical Journal* 132:908-910. DOI: 10.1086/146994.
- Oliphant, T. 2006. *A guide to NumPy* USA: Trelgol Publishing.
- Padovani, P. et al. 2017. “Active Galactic Nuclei: What’s in a Name?” *Annual Review of Astronomy and Astrophysics* 25: Article number 2. DOI: 10.1007/s00159-017-0102-9.
- Paris, I. et al. 2018. “The Sloan Digital Sky Survey Quasar Catalog: Fourteenth Data Release.” *Astronomy and Astrophysics* 613:A51. DOI: 10.1051/0004-6361/201732445.
- Planck Collaboration, et al. 2016. “Planck 2015: Paper XIII. Cosmological parameters”. *Astronomy and Astrophysics* 594:A13. DOI: 10.1051/0004-6361/201525830.
- Rocca-Volmerage, B. et al. 2004. “The Radio Galaxy $K-z$ Relation: The 10^{12} M_\odot mass limit.” *Astronomy and Astrophysics* 415:931-940. DOI: 10.1051/0004-6361:20031717.
- Sanders, D. et al. 1988. “Ultraluminous Infrared Galaxies and the Origin of Quasars.” *The Astrophysical Journal* 325:74-91. DOI: 10.1086/165983.
- Saxena, A. et al. 2018a. “Discovery of a Radio Galaxy at $z = 5.72$.” *Monthly Notices of the Royal Astronomical Society* 480:2733-2742. DOI: 10.1093/mnras/sty1996.
- Saxena, A. et al. 2018b. “Modelling the Luminosities and Sizes of Radio Sources: Radio Luminosity Function at $z = 6$.” *Monthly Notices of the Royal Astronomical Society* 469(4): 4083-4094. DOI: 10.1093/mnras/stx1150.

- Saxena, A. et al. 2019a. "A Search for Faint High-redshift Radio Galaxy Candidates at 150 MHz". *Monthly Notices of the Royal Astronomical Society* 475(4):5041-5058. DOI: 10.1093/mnras/sty152.
- Saxena, A. et al. 2019b. "The Nature of Faint Radio Galaxies at High Redshifts." *Monthly Notices of the Royal Astronomical Society* 489(4):5053-5075. DOI: 10.1093/mnras/stz2516.
- Seymour, N. et al. 2007. "The Massive Hosts of Radio Galaxies across Cosmic Time." *Astrophysical Journal Supplement Series* 171:353-375. DOI: 10.1086/517887.
- Seymour, N. et al. 2008. "Mid-Infrared Spectra of High-Redshift ($z > 2$) Radio Galaxies". *The Astrophysical Journal Letters* 681(1):L1. DOI: 10.1086/590081.
- Spinrad, H. 1982. "Redshifts and spectroscopy of very distant radio galaxies with strong emission lines." *Publications of the Astronomical Society of the Pacific* 94:397-403. DOI: 10.1086/130999.
- Spinrad, H. et al. 1985. "Strong Lyman-alpha emission in three distant radio galaxies." *The Astrophysical Journal* 299:L7-L11. DOI: 10.1086/184570.
- Tielens, A. et al. 1979. "Westerbork Observations of 4C Sources with Steep Radio Spectra." *Astronomy and Astrophysics Supplement Series* 35: 153-162.
- Tingay, S. et al. 2013. "The Murchison Widefield Array: The Square Kilometre Array Precursor at Low Radio Frequencies." *Publications of the Astronomical Society of Australia* 30:e007. DOI: 10.1017/pasa.2012.007.
- Urry, C. and P. Padovani. 1995. "Unified Schemes for Radio-Loud Active Galactic Nuclei." *Publications of the Astronomical Society of the Pacific* 107:803-845. DOI: 10.1086/133630.
- van Breugel, W. et al. 1998. "Morphological Evolution in High-Redshift Radio Galaxies and the Formation of Giant Elliptical Galaxies." *The Astrophysical Journal* 502(2):614-629. DOI: 10.1086/305925.
- van Breugel, W. et al. 1999. "A Radio Galaxy at $z = 5.19$." *The Astrophysical Journal* 518(2):L61-L64. DOI: 10.1086/312080.
- Wayth, R. et al. 2015. "GLEAM: The GaLactic and Extragalactic All-Sky MWA Survey." *Publications of the Astronomical Society of Australia* 32:e025. DOI: 10.1017/pasa.2015.26.

Appendix A

VIKING Inspection Data

The following pages contain tables created during visual comparison of GLEAM high-redshift radio galaxy candidates against VIKING near-infrared (K -band) imaging. For high resolution comparison, VIKING images were compared against radio images obtained from the ASKAP, FIRST, GLASS and VLASS surveys.

Values for RA, DEC, α , β and S_{151} MHz have been rounded down to 3 significant figures.

See Chapters 3 and 4 for further details, including survey fields, methodology and results of NIR visual inspection.

- Table A.1: G1_EQU_GAMA (VLASS, FIRST, VIKING)
- Table A.2: G1_EQU_not_GAMA (FIRST, VIKING)
- Table A.3: G2_SGP_GAMA_VIKING (ASKAP, GLASS, VIKING)

Table A.1: G1_EQU_GAMA (VLASS, FIRST, VIKING).

Name	RA ($^{\circ}$)	Dec ($^{\circ}$)	S_{451} (Jy)	α	β	FIRST morphology	Present	Other VIKING sources $\leq 5''$	Other VIKING sources $\leq 20''$	Single Component?	Multi-Component?	Compact ($\leq 5''$)	Extended ($\geq 5''$)
GLEAM J083609-010838	129.04	-1.143	0.081	-1.461	-2.207	double	Y	N	Y	N	Y	N	Y
GLEAM J083728+002031	129.373	0.345	0.113	-1.422	-1.787	compact	N	N	Y	Y	Y	N	N
GLEAM J084256-015722	130.737	-1.957	0.416	-0.936	-0.646	compact	N	N	Y	Y	Y	N	Y
GLEAM J084340+001313	130.92	0.22	0.547	-1.058	-0.927	double	N	N	Y	Y	Y	N	N
GLEAM J085022-011850	132.596	-1.313	0.133	-1.127	-2.291	double	N	N	Y	Y	Y	N	Y
GLEAM J085557-000055	133.088	-0.016	0.526	-0.929	-0.561	compact	Y	Y	Y	Y	Y	N	N
GLEAM J085614+022359	134.061	2.4	0.894	-1.007	-1.03	compact	N	N	Y	Y	Y	N	N
GLEAM J090060-010227	137.277	-1.041	0.24	-0.823	-1.526	compact	N	N	Y	Y	Y	N	N
GLEAM J090942-015409	137.426	-1.901	0.78	-0.933	-1.419	compact	N	N	Y	Y	Y	N	N
GLEAM J091225-005352	138.105	-0.895	0.291	-1.365	-1.144	double	N	N	Y	Y	Y	N	N
GLEAM J091402+000744	138.513	0.13	0.21	-0.984	-0.727	slightly extended	N	N	Y	Y	Y	N	N
GLEAM J091559-001824	138.998	-0.304	0.08	-0.818	-3.755	compact	Y	Y	Y	Y	Y	N	N
GLEAM J091734-001243	139.393	-0.212	0.465	-0.993	-1.351	compact	N	N	Y	Y	Y	N	N
GLEAM J091921+001608	139.839	0.268	0.307	-0.716	-0.874	compact	Y	Y	Y	Y	Y	N	N
GLEAM J092052+000551	140.218	0.097	0.141	-1.612	-3.028	double	N	N	Y	Y	Y	N	N
GLEAM J092123+013834	140.351	1.643	0.509	-0.764	-0.609	double	N	N	Y	Y	Y	N	N
GLEAM J113720-000447	174.335	-0.079	0.269	-1.064	-2.105	double	N	N	Y	Y	Y	N	N
GLEAM J114010+003356	175.044	0.566	0.120	-0.824	-5.451	double	Y	Y	Y	Y	Y	N	N
GLEAM J114103-015846	175.264	-1.979	0.104	-1.173	-3.366	compact	N	N	Y	Y	Y	N	N
GLEAM J114553-023722	176.473	-2.622	0.142	-0.844	-2.174	compact	Y	Y	Y	Y	Y	N	N
GLEAM J114641-000734	176.672	-0.126	0.57	-0.879	-0.456	double	N	N	Y	Y	Y	N	N
GLEAM J114812+003816	177.048	0.643	0.107	-1.145	-5.315	compact	N	N	Y	Y	Y	N	N
GLEAM J115604+001308	179.019	0.221	0.168	-0.859	-1.643	compact	Y	Y	Y	Y	Y	N	N
GLEAM J115608-003249	179.788	-0.546	0.067	-0.783	-4.448	double	N	N	Y	Y	Y	N	N
GLEAM J121103-025603	182.764	-2.934	0.304	-0.955	-1.351	compact	N	N	Y	Y	Y	N	N
GLEAM J121722-021839	184.345	-2.311	0.134	-0.72	-3.222	compact	Y	Y	Y	Y	Y	N	N
GLEAM J140710-004924	211.794	-0.825	0.311	-1.236	-1.185	compact	N	N	Y	Y	Y	N	N
GLEAM J140851+011218	212.213	1.207	0.065	-1.929	-3.03	compact	N	N	Y	Y	Y	N	N
GLEAM J141023+025958	212.598	3	0.222	-0.934	-2.903	compact	Y	Y	Y	Y	Y	N	N
GLEAM J141026-004152	212.608	-0.698	0.836	-1.16	-0.847	compact	N	N	Y	Y	Y	N	N
GLEAM J141123+004235	212.848	0.71	1.581	-1.141	-0.611	triple	Y	Y	Y	Y	Y	N	N
GLEAM J141554+021029	213.975	2.175	0.434	-0.867	-1.262	double	N	N	Y	Y	Y	N	N
GLEAM J141604+002914	214.017	0.488	0.944	-1.096	-0.823	double	Y	Y	Y	Y	Y	N	N
GLEAM J142417+010957	216.073	1.165	0.144	-1.774	-1.528	compact	N	N	Y	Y	Y	N	N
GLEAM J142550-003605	217.457	-0.605	0.152	-0.89	-2.345	compact	Y	Y	Y	Y	Y	N	N
GLEAM J143227+014303	219.363	1.717	2.399	-0.97	-0.647	slightly extended	N	N	Y	Y	Y	N	N
GLEAM J143800+002327	219.504	0.39	1.019	-1.267	-1.819	compact	N	N	Y	Y	Y	N	N
GLEAM J144118+002507	220.331	0.419	0.613	-1.306	-1.84	extended	Y	Y	Y	Y	Y	N	N
GLEAM J144305+022940	220.771	2.494	0.211	-0.744	-2.561	compact	N	N	Y	Y	Y	N	N
GLEAM J144911-013119	222.297	-1.522	1.264	-0.993	-0.45	double	Y	Y	Y	Y	Y	N	N

Table A.2: G1EQU_not_GAMA (FIRST, VIKING).

Name	RA (°)	Dec (°)	S_{151} (Jy)	α	β	FIRST morphology	Present in VIKING	Single Component?	Multi-Component?	Compact ($\leq 5''$)	Extended ($\geq 5''$)
GLEAM J103055+013519	157.73	1.59	0.205	-0.81	-2.179	Compact	N	Y	N	Y	N
GLEAM J103223+033933	158.099	3.661	0.917	-1.118	-0.541	Compact	N	Y	N	Y	N
GLEAM J103311-035333	158.298	-3.892	0.685	-0.741	-0.5	Extended	N	Y	N	Y	Y
GLEAM J103340+010725	158.42	1.126	0.416	-0.91	-0.742	Compact	N	Y	N	Y	N
GLEAM J103345+031030	158.438	3.176	0.782	-0.97	-0.39	Double	N	Y	N	Y	Y
GLEAM J103423-033507	158.509	-3.585	0.147	-0.958	-2.577	Compact	Y	Y	N	Y	N
GLEAM J103535-033344	158.896	-3.562	1.034	-0.789	-0.696	Extended	Y	Y	N	Y	Y
GLEAM J103747-032519	159.447	-3.418	0.15	-0.904	-2.771	Compact	N	Y	N	Y	N
GLEAM J103822+012122	159.594	1.358	0.645	-0.774	-0.775	Compact	Y	Y	N	Y	N
GLEAM J103938+002823	159.914	0.472	0.327	-1.12	-1.334	Compact	Y?	N	Y	Y	N
GLEAM J104041+015003	160.173	1.835	0.413	-1.294	-0.778	Compact	N	Y	N	Y	Y
GLEAM J104056+005514	160.234	0.923	0.273	-0.754	-0.716	Compact	Y	Y	N	Y	N
GLEAM J104335+011621	160.9	1.274	0.596	-0.951	-0.496	Extended	Y	Y	N	Y	Y
GLEAM J104443-034100	161.178	-3.682	0.086	-0.869	-6.697	Compact	N	Y	N	Y	N
GLEAM J104804-025538	162.021	-2.927	0.302	-0.756	-1.431	Compact	Y	Y	N	Y	N
GLEAM J104906-024558	162.279	-2.76	0.481	-0.789	-0.974	Extended	N?	N	Y	Y	N
GLEAM J104959+001304	162.496	0.219	1.222	-0.941	-0.538	Compact	Y	Y	N	Y	Y
GLEAM J105232-031808	163.133	-3.301	0.166	-1.081	-1.918	Compact	N?	N	Y	Y	N
GLEAM J105325+011226	163.355	1.209	0.275	-0.955	-1.746	Extended	Y	Y	N	Y	Y
GLEAM J105620+010757	164.085	1.134	0.17	-1.072	-1.935	Compact	N?	N	Y	Y	?
GLEAM J110150-005125	165.163	-0.856	0.252	-1.252	-2.47	Compact	Y	Y	N	Y	N
GLEAM J110254-024333	165.729	-2.726	1.393	-0.925	-0.677	Extended	Y	Y	N	Y	N
GLEAM J110345+011402	165.937	1.235	0.305	-0.922	-0.656	Compact	Y	Y	N	Y	Y
GLEAM J110358+030059	165.993	3.018	0.734	-1.066	-0.336	Compact	Y?	N	Y	Y	N
GLEAM J110441-002035	166.169	-0.342	0.086	-0.966	-1.558	Extended	Y	Y	N	Y	?
GLEAM J110631+013431	166.631	1.576	0.767	-0.751	-1.108	Compact	Y	Y	N	Y	N
GLEAM J110641+014123	166.674	1.69	0.123	-1.071	-5.44	Compact	Y	Y	N	Y	N
GLEAM J111012+011712	167.552	1.287	0.356	-0.925	-0.677	Extended	Y?	N	Y	Y	N
GLEAM J111023+005606	167.559	0.935	0.243	-0.925	-0.656	Extended	Y	Y	N	Y	Y
GLEAM J111043+020218	167.679	2.039	0.088	-0.935	-0.208	Compact	Y?	N	Y	Y	N
GLEAM J111122-033324	167.844	-3.555	0.431	-0.966	-0.962	Extended	Y	Y	N	Y	N
GLEAM J111211+005607	168.043	0.94	0.168	-0.931	-1.947	Compact	Y?	N	Y	Y	N
GLEAM J111215+012037	168.065	1.343	0.455	-0.79	-0.762	Extended	Y	Y	N	Y	N
GLEAM J111619+012927	168.082	1.488	0.499	-1.113	-1.403	Extended	Y	Y	N	Y	N
GLEAM J111819-024207	168.832	-2.701	0.586	-0.961	-1.339	Extended	Y	Y	N	Y	Y
GLEAM J112023+002501	170.098	0.417	0.185	-0.805	-3.446	Compact	Y	Y	N	Y	N
GLEAM J112250+014957	170.712	1.833	0.592	-0.952	-0.424	Extended	Y	Y	N	Y	?
GLEAM J112421+020328	171.019	2.059	0.522	-0.958	-0.485	Extended	Y	Y	N	Y	N
GLEAM J112557-034203	171.489	-3.701	0.511	-0.931	-0.333	Compact	N	Y	N	Y	N
GLEAM J112706-033210	171.779	-3.358	0.326	-1.224	-0.779	Compact	N	Y	N	Y	N
GLEAM J112747+034103	171.948	3.685	1.018	-1.002	-0.23	Extended	Y	Y	N	Y	Y
GLEAM J112755-005514	171.978	-0.919	0.692	-0.722	-0.54	Extended	?	N	Y	Y	?
GLEAM J113053-020723	172.723	-2.122	0.21	-0.738	-1.486	Compact	Y?	N	Y	Y	N
GLEAM J113407+022809	173.531	2.469	0.35	-1.035	-1.131	Extended?	Y?	N	Y	Y	?
GLEAM J113601-035122	174.007	-3.855	0.193	-0.809	-1.314	Compact	N	Y	N	Y	?
GLEAM J113610+031742	174.045	2.6	0.211	-0.712	-1.259	Compact	Y?	N	Y	Y	N
GLEAM J112455-030726	174.146	-3.124	0.263	-0.756	-3.292	Compact	N	Y	N	Y	?
GLEAM J112755-005174	174.571	-0.295	0.313	-0.703	-1.531	Compact	N	Y	N	Y	N
GLEAM J130748+020837	196.935	2.143	0.489	-0.825	-0.616	Compact	Y?	N	Y	Y	N
GLEAM J131347-010225	198.449	-1.041	0.324	-0.942	-0.924	Extended	Y	Y	N	Y	N
GLEAM J131442+004955	198.681	0.833	0.224	-1.276	-3.32	Extended?	Y?	N	Y	Y	?
GLEAM J131553+023604	198.975	2.6	0.122	-0.709	-1.95	Compact	Y	Y	N	Y	N
GLEAM J131748+033906	199.451	3.654	0.392	-1.273	-1.005	Compact	N	Y	N	Y	Y
GLEAM J131950-001630	199.963	-0.276	0.255	-0.922	-3.547	Compact	Y?	N	Y	Y	?
GLEAM J132918+013341	202.328	1.561	0.653	-0.914	-0.627	Compact	N	Y	N	Y	N
GLEAM J132953+015212	202.473	1.869	0.566	-0.806	-0.609	Compact	Y	Y	N	Y	N
GLEAM J133236-010148	203.153	-1.03	0.255	-1.278	-1.54	Compact	Y	Y	N	Y	Y
GLEAM J133246-022659	203.194	-2.45	1.141	-0.869	-0.494	Compact	Y	Y	N	Y	N
GLEAM J133329-0333801	203.371	-3.632	0.438	-0.992	-1.027	Extended	N	Y	Y	Y	Y

Table A.2 continued from previous page

Name	RA ($^{\circ}$)	Dec ($^{\circ}$)	S_{151} (Jy)	α	β	FIRST morphology	Present in VIKING	Single Component?	Multi-Component?	Compact ($\leq 5''$)	Extended ($\geq 5''$)
GLEAM J133531+011219	203.88	1.206	0.386	-0.945	-0.973	Compact	N	Y	N	Y	N
GLEAM J133548-014424	203.953	-1.74	0.561	-0.901	-1.196	Extended	Y	N	Y	N	Y
GLEAM J133744+032813	204.134	3.469	0.262	-0.953	-1.31	Compact	N	Y	N	Y	N
GLEAM J133859-024901	204.747	-2.817	0.389	-0.912	-0.555	Extended	Y	N	Y	N	Y
GLEAM J134030+000953	205.129	0.165	0.384	-1.092	-2.039	Compact	Y?	Y	N	Y	N
GLEAM J134407-035203	206.029	-3.868	0.462	-0.89	-0.643	Compact	Y	Y	N	Y	N
GLEAM J134517-034452	206.326	-3.748	0.47	-0.76	-0.526	Extended	Y	N	Y	Y	N
GLEAM J134636-010028	206.653	-1.009	0.447	-0.873	-0.647	Compact	N	Y	N	Y	N
GLEAM J134703+0005051	206.767	0.849	0.019	-0.917	-7.447	Compact	N	Y	N	Y	N
GLEAM J134747+001243	206.947	0.212	0.535	-0.942	-0.501	Compact	N?	Y	N	Y	N
GLEAM J134757+013034	206.99	1.512	0.186	-1.393	-3.565	Extended	Y	N	Y	N	Y
GLEAM J134912+022200	207.303	2.367	0.242	-0.979	-1.648	Compact	N	Y	N	Y	N
GLEAM J135158-020956	207.991	-2.166	2.503	-0.958	-0.383	Compact	N	Y	N	Y	N
GLEAM J140021+003021	210.089	0.506	2.669	-1.019	-0.543	Compact	N	Y	N	Y	N
GLEAM J140137+021507	210.406	2.251	0.243	-1.135	-2.285	Extended?	Y?	Y	N	Y	?
GLEAM J140214+031753	210.562	3.299	0.72	-0.942	-1.143	Compact	Y?	Y	N	Y	N
GLEAM J140410+005949	211.04	0.998	0.267	-0.984	-1.555	Extended	Y	Y	N	Y	N
GLEAM J142732+031533	216.883	3.26	4.427	-0.989	-0.585	Extended	Y	Y	N	Y	N
GLEAM J142742-031547	216.932	-3.26	0.111	-0.719	-3.175	Compact	Y?	Y	N	Y	N
GLEAM J143932+030854	219.886	3.148	0.867	-1.191	-0.724	Extended	Y?	Y	N	Y	N
GLEAM J144553+034730	221.471	1.624	-1.104	-1.152	Extended	N	Y	N	Y	N	Y
GLEAM J144946-021917	222.443	-2.322	0.106	-0.905	-2.374	Compact	Y	Y	N	Y	N
GLEAM J145958+030730	224.993	3.125	0.446	-0.759	-2.331	Compact	?	Y	N	Y	N
GLEAM J150302-013315	225.759	-1.555	0.362	-1.189	-0.97	Compact	Y	Y	N	Y	N
GLEAM J151200-011734	228.002	-1.292	0.237	-0.921	-1.053	Extended?	Y?	Y	N	Y	N
GLEAM J151440-013502	228.672	-1.584	0.154	-1.313	-2.932	Compact	Y	Y	N	Y	N
GLEAM J152154-010413	230.478	-1.071	0.11	-1.302	-3.496	Compact	N	Y	N	Y	N
GLEAM J152623+010957	231.597	1.165	2.247	-1.016	-0.73	Compact	Y	Y	N	Y	N
GLEAM J152809+015342	232.041	1.895	0.066	-0.995	-0.494	Compact	Y	Y	N	Y	N
GLEAM J153442-012128	233.68	-1.36	0.148	-1.104	-2.646	Compact	N?	N	N	Y	N
GLEAM J154219-033859	235.583	-0.65	0.852	-0.957	-1.119	Extended	Y	Y	N	Y	N

Table A.3: G2_SGP_GAMA_VIKING (ASKAP, GLASS, VIKING).

Name	RA ($^{\circ}$)	Dec ($^{\circ}$)	S_{151} (Jy)	α	β	ASKAP morphology	GLASS morphology	Present in VIKING	Other VIKING sources $\leq 5''$	Single Component?	Multi-component?	Compact ($\leq 5''$)	Extended ($\geq 5''$)
GLEAM_J223931-340421	339.883	-34.074	0.405	-0.987	-0.281	double	double	Y	Y	N	Y	N	Y
GLEAM_J224145-340618	340.44	-34.106	0.198	-0.771	-0.55	single	extended	Y	Y	Y	Y	N	Y
GLEAM_J225106-322012	342.777	-32.335	0.058	-0.913	-4.283	extended	extended	Y	Y	?	N	N	Y
GLEAM_J225511-302547	343.796	-30.429	3.664	-1.016	-0.403	not present	lobe	N	Y	N	N	N	Y
GLEAM_J225912-311114	344.798	-31.185	0.092	-1.093	-1.197	extended	extended	N	Y	N	N	N	Y
GLEAM_J225934+304438	344.895	-30.745	0.305	-0.91	-0.312	double	triple	Y	Y	Y	Y	N	Y
GLEAM_J230031-342301	345.133	-34.383	0.074	-1.01	-1.547	double	double	Y	Y	N	Y	N	Y
GLEAM_J230048+232321	345.203	-32.543	0.337	-0.811	-0.683	double	double	Y	Y	N	Y	N	Y
GLEAM_J230202-314935	345.51	-31.827	0.089	-1.031	-1.341	single	single	Y	Y	N	Y	N	Y
GLEAM_J230306-304050	345.782	-30.679	0.079	-1.353	-1.68	double	double	Y	Y	N	Y	N	Y
GLEAM_J230505-222311	346.272	-32.388	0.722	-1.165	-0.407	single	single	N	Y	Y	Y	N	Y
GLEAM_J230606-324410	346.501	-32.738	0.302	-0.986	-0.367	single	extended	Y	Y	Y	Y	N	Y
GLEAM_J230633-301315	346.64	-30.221	1.458	-0.862	-0.269	extended	extended	N	Y	?	?	N	Y
GLEAM_J230736-310118	346.904	-31.024	0.321	-0.868	-0.807	single	single	Y	Y	N	Y	N	Y
GLEAM_J230816-312058	347.069	-31.35	0.092	-1.201	-1.388	double	double	Y	Y	N	Y	N	Y
GLEAM_J230845-315210	347.187	-31.868	0.045	-0.855	-3.189	single	single	Y	Y	N	Y	N	Y
GLEAM_J230954-222709	347.477	-32.454	0.064	-1.178	-1.584	single	single	N	Y	Y	Y	N	Y
GLEAM_J231014-341517	347.562	-34.256	0.142	-0.94	-1.342	single	compact	Y	Y	Y	Y	N	Y
GLEAM_J231050-312912	347.712	-31.486	0.104	-0.948	-1.016	single	compact	Y	Y	Y	Y	N	Y
GLEAM_J231106-301059	347.751	-30.284	0.303	-0.92	-0.598	extended	compact	Y	Y	N	Y	N	Y
GLEAM_J231106-311019	347.754	-31.17	0.065	-0.897	-0.917	double	double	Y	Y	N	Y	N	Y
GLEAM_J231139-313805	347.916	-31.635	0.076	-0.964	-1.513	extended	extended	Y	Y	N	Y	N	Y
GLEAM_J231139-3223621	348.142	-32.608	0.067	-0.772	-3.395	not resolved	not resolved	Y	Y	N	Y	N	Y
GLEAM_J231322-324426	348.344	-32.741	0.247	-0.983	-0.394	double	double	N	Y	N	Y	N	Y
GLEAM_J231519-315158	348.83	-31.867	0.533	-1.152	-0.37	extended	extended	Y	Y	N	Y	N	Y
GLEAM_J231707-321757	349.281	-32.3	0.165	-0.957	-0.784	double	double	Y	Y	N	Y	N	Y
GLEAM_J231834-321815	349.646	-32.306	0.084	-0.989	-1.371	double	double	Y	Y	N	Y	N	Y
GLEAM_J231845-322118	349.69	-32.357	1.206	-1.006	-0.421	extended	extended	N	Y	N	Y	N	Y
GLEAM_J231904-334826	349.769	-33.809	0.577	-1.109	-0.343	double	double	N	Y	N	Y	N	Y
GLEAM_J231941-343852	349.926	-34.648	0.092	-1.315	-1.273	double	double	Y	Y	N	Y	N	Y
GLEAM_J231949-312445	349.954	-31.413	0.068	-1.38	-1.793	single	compact	N	Y	N	Y	N	Y
GLEAM_J232008-300444	350.037	-30.079	0.227	-0.962	-0.554	extended	extended	Y	Y	N	Y	N	Y
GLEAM_J232035-320231	350.149	-32.042	0.307	-0.712	-0.301	extended	extended	Y	Y	N	Y	N	Y
GLEAM_J232213-313801	350.555	-31.638	0.15	-0.984	-0.836	extended	extended	N	Y	N	Y	N	Y
GLEAM_J232256-3341105	350.709	-34.185	0.129	-0.89	-0.978	double	double	N	Y	N	Y	N	Y